Journal of
Marine Science
and Engineering

Article

Investigation of Structural Nonlinearity Effects on the Aeroelastic and Wake Characteristics of a 15 MW Wind Turbine

Zhenju Chuang [1], Lulin Xia [1,*], Yan Qu [2], Wenhua Li [3] and Jiawen Li [4]

[1] Naval Architecture and Ocean Engineering College, Dalian Maritime University, Dalian 116026, China; zhenjuchuang@dlmu.edu.cn
[2] School of Marine Science and Engineering, South China University of Technology, Guangzhou 511442, China; quyan@scut.edu.cn
[3] Marine Engineering College, Dalian Maritime University, Dalian 116026, China; lwh992@dlmu.edu.cn
[4] Navigation College, Dalian Maritime University, Dalian 116026, China; lijiawen@dlmu.edu.cn
* Correspondence: xialulin@dlmu.edu.cn

Abstract: As wind turbines increase in size, blades become longer, thinner, and more flexible, making them more susceptible to large geometric nonlinear deformations, which pose challenges for aeroelastic simulations. This study presents a nonlinear aeroelastic model that accounts for large deformations of slender, flexible blades, coupled through the Actuator Line Method (ALM) and Geometrically Exact Beam Theory (GEBT). The accuracy of the model is validated by comparing it with established numerical methods, demonstrating its ability to capture the bending–torsional coupled nonlinear characteristics of highly flexible blades. A bidirectional fluid–structure coupling simulation of the IEA 15MW wind turbine under uniform flow conditions is conducted. The effect of blade nonlinear deformation on aeroelastic performance is compared with a linear model based on Euler–Bernoulli beam theory. The study finds that nonlinear deformations reduce predicted angle of attack, decrease aerodynamic load distribution, and lead to a noticeable decline in both wind turbine performance and blade deflection. The effects on thrust and edgewise deformation are particularly significant. Additionally, nonlinear deformations weaken the tip vortex strength, slow the momentum exchange in the wake region, reduce turbulence intensity, and delay wake recovery. This study highlights the importance of considering blade nonlinear deformations in large-scale wind turbines.

Keywords: wind turbine; aeroelastic responses; fluid–structure interaction; large-eddy simulation; nonlinear beam

check for updates

Academic Editor: Eugen Rusu

Received: 1 December 2024
Revised: 7 January 2025
Accepted: 8 January 2025
Published: 10 January 2025

Citation: Chuang, Z.; Xia, L.; Qu, Y.; Li, W.; Li, J. Investigation of Structural Nonlinearity Effects on the Aeroelastic and Wake Characteristics of a 15 MW Wind Turbine. *J. Mar. Sci. Eng.* **2025**, *13*, 116. https://doi.org/10.3390/jmse13010116

1. Introduction

With the increasing demand for clean and renewable energy, the size of offshore wind turbines continues to grow, and the length of their blades is constantly pushing new limits. Due to the weight constraints of megawatt-class turbines and the use of lightweight composite materials such as fiberglass, the blades are designed to be longer, lighter, and more flexible [1,2]. This makes the blades more susceptible to strong wind loads and large deflections, which in turn cause significant deformations [3], which in turn affect the dynamic response and aerodynamic performance of wind turbines [4]. Therefore, investigating the aeroelastic effects of large wind turbine blades is of great importance [5,6]. For large wind turbines with long, flexible blades, even under rated operating conditions, large deformations may induce geometric nonlinearities in the structure [7], which significantly impact the structural and aeroelastic behavior [3]. It is essential to further investigate the influence of geometric nonlinear deformations of blades on the aeroelastic response of wind turbines, particularly the nonlinear coupling effects between blade stretching, bending, and torsion. Therefore, it is necessary to develop an aeroelastic model for large blades that accounts for the associated structural geometric nonlinearities. Furthermore, the changes in blade loading and deformation caused by aeroelastic effects in wind turbines can influence the location of vortex emission at the blade tip [8–10], and significantly influence the wake recovery in the far-wake region [11]. These changes are crucial for optimizing wind farm layouts [12], making it necessary to study the wake considering blade deformations.

The main challenge in aeroelastic simulations of wind turbines is selecting appropriate aerodynamic and structural models, which vary depending on the focus of the simulation. For aerodynamic modeling of wind turbines with large, flexible blades, it is crucial to consider the effects of blade deformation and vibration on the wake [9]. The widely used Blade Element Momentum Theory (BEMT) offers high efficiency and accuracy but fails to provide detailed information on wake aerodynamics. Other medium-accuracy models, such as the Vortex Lattice Model (VLM) [13], lifting line theory (LLT) [14], and vortex-based panel methods [15], have certain limitations when dealing with far-wake or complex unsteady wake effects. With the advancement of high-performance computing technologies, Computational Fluid Dynamics (CFD) has been widely used for high-fidelity aerodynamic simulations [8,16,17]. However, simulating large-scale rotors with diameters on the order of 100 m still requires significant computational resources and time costs. Therefore, the Actuator Line Model (ALM) [18], which combines the advantages of CFD and BEMT, has been proposed. The ALM models the blade using virtual actuator lines, without directly solving the actual flow around the blades, thus effectively modeling the three-dimensional wake dynamics. This model has been shown to effectively and accurately reproduce the flow field of wind turbines and has been widely applied in studies of atmospheric turbulence boundary layers [19,20], wake interaction analysis between multiple wind turbines [21,22], and aeroelasticity research [23,24].

In the structural modeling of wind turbine blades, the most commonly used methods are the three-dimensional finite element model (3DFEM) and the one-dimensional equivalent beam model (EBM) [25]. For structural dynamic simulations of large wind turbines, the 3DFEM is computationally expensive, whereas the equivalent beam model is considered efficient and capable of providing reasonable accuracy [26]. To discretize the blade into a series of one-dimensional beam elements, modal methods, Multi-Body Dynamics (MBD), and Finite Element Methods (FEMs) are commonly used. As the blade size and complexity increase, most traditional linear methods based on small deformation assumptions become inapplicable [27]. MBD requires an increase in the number of sub-bodies used to accurately capture more pronounced nonlinear effects [28]. In contrast, the one-dimensional Finite Element Method (1DFEM) demonstrates the highest accuracy in dynamic response, providing a more comprehensive and accurate description of wind turbine blade deformations, although it requires slightly more computational resources [5]. However, for slender, flexible blades experiencing large deflection deformations, the current 1D FEM method based on small-deflection beam theory may no longer be applicable [3]. To address the geometric nonlinearities in highly flexible blades, the Geometrically Exact Beam Theory provides an effective solution. This theory accounts for the six-degree-of-freedom coupling effects of the blade, accurately describing large structural displacements and rotations, and solving the dynamic response of the blade under large deflections. It has been widely applied in the nonlinear structural modeling of wind turbines [29–31].

The coupling of structural and aerodynamic models has driven the development of various integrated aeroelastic frameworks. Wang et al. [26] developed a nonlinear aeroelastic model based on BEM and Geometrically Exact Beam Theory (GEBT), observing a reduction in the sway deflections predicted by the nonlinear aeroelastic model. Sabale and Gopal [32] used BEM and GEBT to study the nonlinear aeroelastic response under turbulent conditions. Yu and Kwon [16] used the high-fidelity CFD-CSD method to study the aeroelastic response, taking into account the interaction effects of the tower and rotor tilt angle, and found that aeroelastic deformation significantly reduced aerodynamic loads on the blades. Liu et al. [33] employed a CFD and Multi-Body Dynamics (MBD) coupling method to model the blades and investigate the effects of platform motion and blade deformation on the structural responses and aerodynamic characteristics of the wind turbine. Höning et al. [34] used CFD-GEBT to study the near-wake region of the rotor and found that blade deformation leads to uneven wake characteristics in terms of velocity and shape. Ma et al. [35] used the ALM combined with a finite element model to study the aeroelastic behavior of wind turbine blades, accounting for the nonlinear effects of blade deformation. They pointed out that neglecting wind turbine deformation leads to an underestimation of the velocity and vorticity recovery in the far-wake region. Meng et al. [23] used ALM combined with a one-dimensional equivalent beam model to study wake interactions between wind turbines. Huang et al. [36] coupled ALM with the equivalent beam model to investigate the effects of blade deformations on the aerodynamic loads and wake of the wind turbine under varying inflow conditions. They found that the angle of attack (AOA) of the blades was significantly altered due to torsional deformations, thereby having a significant impact on the aerodynamic loads on the wind turbine. Trigaux et al. [10] developed a nonlinear aeroelastic model by coupling Geometrically Exact Beam Theory (GEBT) with the Flexible Actuator Line Method, investigating the load variations and wake effects induced by blade flexibility. However, due to the negligible effects of torsion, elongation, and shear in the NREL-5MW model [31,37], the studies mentioned above have certain limitations. Many of these studies [4,6,9,16,23,35,36] focus on the NREL-5MW turbine, neglecting the nonlinear effects induced by large displacements. Moreover, the wake changes resulting from large deflection deformations should be further investigated.

The aim of this study is to propose a bidirectionally coupled nonlinear aeroelastic model that integrates ALM and GEBT, capable of considering large geometric deformations of slender flexible blades. The model is used to investigate the impact of nonlinear effects on aeroelastic behavior and to predict blade loads and their effects on the wake. The nonlinear aeroelastic model is validated through comparisons with OpenFAST and existing studies. Additionally, by applying it to the aeroelastic modeling of the IEA-15MW wind turbine, the influence of nonlinear effects on aerodynamic loads, blade deformations, and wake dynamics is assessed, and a comparative analysis with linear models is performed.

The structure of this paper is as follows: Section 2 presents the fundamental theory of the aeroelastic model. Section 3 provides a detailed description of the simulation setup and conducts a sensitivity analysis. Section 4 presents extensive validation of the nonlinear aeroelastic model, along with a comparison of its numerical simulations against those of the linear model. Section 5 summarizes the main findings of this study and outlines potential future developments.

2. Numerical Methods

This section introduces and discusses the theoretical methods and numerical implementation of the selected aerodynamic model and the nonlinear equivalent beam model. The aerodynamic model and the structural model are implemented using the open-source solvers OpenFOAM-6 and BeamDyn [31], respectively. The loosely coupled fluid–structure solver scheme is improved and implemented based on the open-source tool SOWFA [19] developed by NREL. SOWFA is a high-fidelity wind field modeling tool developed by the

National Renewable Energy Laboratory (NREL), and previous studies [20,22,38,39] have demonstrated the reliability of this tool.

2.1. Governing Equation

The LES method is used to describe the wind flow field around the wind turbine, solving the spatially filtered continuity and incompressible Navier–Stokes equations, as follows:

$$\frac{\partial \overline{u}_i}{\partial x_i} = 0 \tag{1}$$

$$\frac{\partial \overline{u}_i}{\partial t} + \frac{\partial}{\partial x_i}\left(\overline{u}_i \overline{u}_j\right) = -\frac{1}{\rho}\frac{\partial \overline{p}}{\partial x_i} + v\nabla^2 \overline{u_i} - \frac{\partial \tau_{ij}}{\partial x_j} + f_i \tag{2}$$

Here, u represents the filtered velocity, p represents the filtered pressure, and spatial filtering is performed using a box filter, which is implemented through a uniform weighted average over the grid cells. ρ is the air density, v is the kinematic viscosity, and ∇^2 is the Laplacian operator. f_i denotes the body force generated by the wind turbine Actuator Line Model. τ_{ij} is the anisotropic part of the subgrid-scale (SGS) stress tensor introduced by the filtering operation, and is modeled using the Smagorinsky SGS model, as follows:

$$\tau_{ij} - \frac{1}{3}\tau_{kk}\delta_{ij} = -2\mu_t \overline{S}_{ij} \tag{3}$$

Here, $\bar{\mathrm{S}}_{\mathrm{ij}} = \frac{1}{2}\left(\frac{\partial \overline{u}_i}{\partial x_j} + \frac{\partial \overline{u}_j}{\partial x_i}\right)$ represents the filtered strain rate tensor, μ_t is calculated as $u_t = (C_S\Delta)^2|\bar{S}_{ij}$, the calculated eddy viscosity, and the estimate of μ_t is based on Prandtl's mixing length theory [21,22]. C_S represents the mixing characteristic length, and Δ is the filter size, taken as the cube root of the cell volume ($\Delta = \sqrt[3]{\Delta_x \Delta_y \Delta_z}$ for Cartesian grids). The magnitude of the resolved strain rate tensor is given by $\left|\bar{S}_{ij}\right| = \sqrt{2\bar{S}_{ij}\bar{S}_{ij}}$, assuming that the turbulence is homogeneous and isotropic in the inertial subrange, with a Smagorinsky constant of $C_S = 0.168$.

The simulation is based on the incompressible unsteady flow solver pimpleFoam in OpenFOAM. A cell-centered finite volume method is used for spatial discretization, with first-order backward differencing and second-order central differencing applied to compute the time and convection terms, respectively. Furthermore, a second-order scheme with explicit non-orthogonal correction is used for the diffusion terms.

2.2. Actuator Line Model

The wind turbine blades are modeled using the Actuator Line Method (ALM), which was first proposed by [18], due to its effective balance between fidelity and computational resources, it has been widely applied in wind turbine simulations. The ALM replaces the blades with virtual forces, representing the blades as force actuator points based on the momentum of the blade elements. The total force at each actuator point ($f(x)$, where x denotes the actuator point in the ALM model) is calculated as follows:

$$f = \frac{1}{2}\rho c U_{rel}^2 dr(C_l e_l + C_d e_d) \tag{4}$$

c is the local chord length of the blade, e_l and e_d are the unit vectors for lift and drag, while C_l and C_d are the two-dimensional lift and drag coefficients. These values depend on the airfoil type, local angle of attack α, and Reynolds number, and can be obtained from tabulated data [40]. The velocity triangle of the airfoil section at the blade radius r is shown in the Figure 1, where U_{rel} is the relative flow velocity at the local rotating blade, determined by the following formula:

$$U_{rel} = \sqrt{U_0^2 + (U_R - \omega r)^2} \tag{5}$$

U_0 is the sampled velocity obtained from the flow field at each actuator point, determined by linear interpolation of the flow velocity at the grid points [36].

ω is the angular velocity of the rotor, and r represents the distance vector from the hub to the actuator point. The local angle of attack (AOA) α can be obtained using the following formula:

$$\alpha = \varphi - \theta_0 - \theta_p + \theta_e \tag{6}$$

$$\varphi = \arctan(\left(\frac{U_0}{U_R - \omega r}\right)) \tag{7}$$

φ is the local flow inflow angle; θ_0, θ_p, and θ_e represent the initial twist angle, pitch angle, and elastic twist angle of each blade section, respectively. Positive θ_e indicates the upward direction of the nose, pointing in the negative x direction in the interface coordinate system.

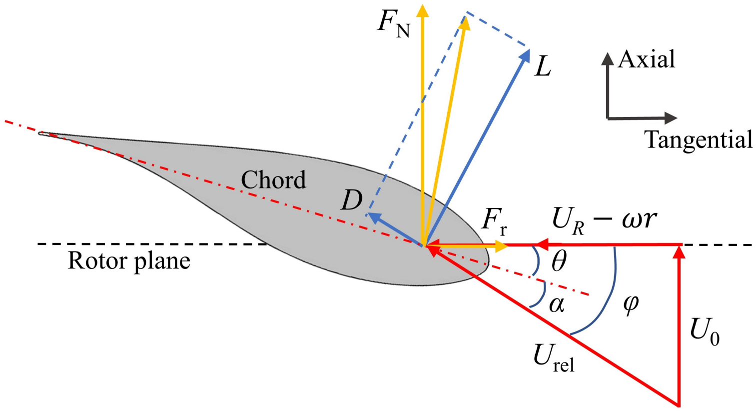

Figure 1. Velocity vectors of an airfoil section.

Additionally, in the ALM, to avoid numerical issues related to singularities, the forces need to be smoothly distributed across multiple grid points, which is typically achieved by convolving the force with a regularization kernel. In this work, a three-dimensional Gaussian kernel is used for this purpose.

$$\eta_\varepsilon(d) = \frac{1}{\varepsilon^3 \pi^{3/2}} \exp\left[-\left(\frac{d}{\varepsilon}\right)^2\right] \tag{8}$$

The Gaussian projection width ε is a key variable for accurately predicting rotor power and wake. The larger the value of ε, the smoother the force distribution and the greater the influence range of the body force. It is crucial for the accurate prediction of rotor power and wake [41–43]. In this study, the relationship between the numerical simulation results based on output power and other parameters and the Gaussian projection width is used to select an appropriate value for ε. Additionally, to account for the three-dimensional effects near the blade root and tip, Glauert's tip loss correction [44] is applied to avoid overestimating the blade tip loads, providing a more accurate representation of the impact of the tip vortex on blade performance.

2.3. Structural Model

The structural model is based on the displacement-based Geometrically Exact Beam Theory (GEBT). In geometric nonlinear analysis, no approximations are made for the geometry before and after deformation. The theory accounts for initial curvature and torsion, and can handle large deformations of the beam axis and large rotations of the beam cross-section. The beam's deformation behavior is described using three coordinate systems: the global coordinate system (A), the reference frame in the undeformed state (B), and the reference frame in the deformed state (C). As shown in Figure 2, the diagram illustrates the beam in both the deformed and undeformed states based on the GEBT theory.

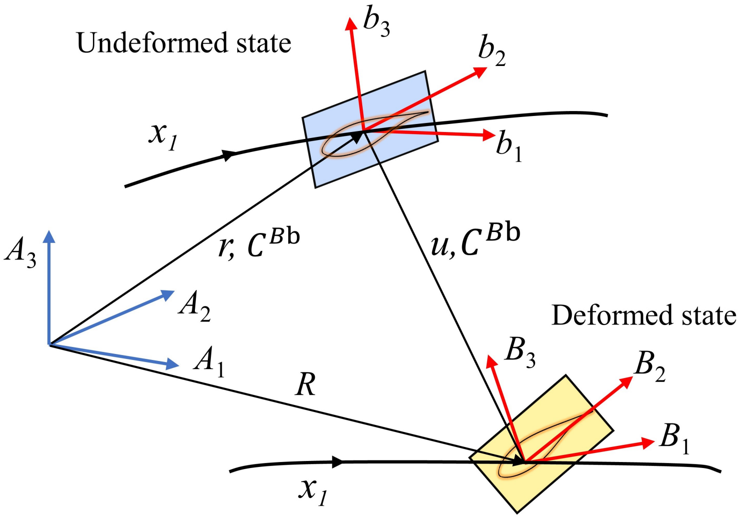

Figure 2. Beam in deformed states.

In the undeformed state, a reference frame b_i is introduced along the beam axis, and a reference frame B_i is introduced for each element along the deformed beam axis. The curvilinear coordinate X_1 is used to define the intrinsic parameterization of the reference line.

The equation of motion for the Geometrically Exact Beam Theory is written as

$$\frac{\partial h}{\partial t} - F' = f \tag{9}$$

$$\frac{\partial g}{\partial t} + \frac{\partial u}{\partial t} h - M' - (x_0' + u')F = m \tag{10}$$

Here, h and g represent the linear momentum and angular momentum, respectively; F' and M' denote the force and moment on the beam cross-section; t is time; u is the one-dimensional displacement along the reference line; x_0 is the position vector of a point along the reference line; f and m represent the distributed force and moment applied to the beam structure; $(\cdot)'$ denotes the derivative of a quantity with respect to the curvilinear coordinate x_1.

Based on the small strain assumption, the relationship between momentum and velocity, as well as strain and sectional forces, is given by

$$\left\{ \begin{array}{c} h \\ g \end{array} \right\} = M_1 \left\{ \begin{array}{c} v \\ \omega \end{array} \right\} \tag{11}$$

$$\left\{ \begin{array}{c} F \\ M \end{array} \right\} = K \left\{ \begin{array}{c} \varepsilon \\ \kappa \end{array} \right\} \tag{12}$$

Here, M_1 and K are the 6 × 6 sectional mass and stiffness matrices; ε and κ are the one-dimensional strain and one-dimensional curvature; v and ω represent the linear velocity and angular velocity, respectively.

The one-dimensional strain and curvature are defined as follows:

$$\left\{ \begin{array}{c} \varepsilon \\ \kappa \end{array} \right\} = \left\{ \begin{array}{c} x_0' + u' - (RR_0)l_1 \\ k \end{array} \right\} \tag{13}$$

Here, R denotes the rotation tensor; R_0 represents the initial rotation tensor; k is the curvature vector of the cross-section; and l_1 is the unit vector along the s direction.

For the displacement-based finite element implementation, space discretization is performed using isoparametric beam elements with two nodes, three nodes, and six degrees of freedom per node. The linearized form of the nonlinear equation of motion is given as follows:

$$\bar{M}_1 \Delta\bar{a} + \bar{G}\Delta\bar{v} + \bar{K}\Delta\bar{q} = \bar{F}_0 - \bar{F}_1 \tag{14}$$

Here, $\bar{M}_1$, $\bar{G}$ and $\bar{K}$ represent the element mass, gyroscopic, and stiffness matrices, respectively; $\Delta\bar{a}$, $\Delta\bar{v}$ and $\Delta\bar{q}$ represent the increments of the generalized element acceleration, velocity, and displacement arrays, respectively; $\bar{F}_0$ denotes the externally applied load; $\bar{F}_1$ represents the element forces; $\overline{(\cdot)}$ denotes the linearized form of the terms in the equations. The linearized equation of motion is solved using the second-order accurate generalized-α time integration scheme, which allows the introduction of integration parameters for high-frequency numerical dissipation [31].

The parameterization of rotation is carried out using the Wiener–Milenkovic parameter, which effectively accounts for the gyroscopic effect and centrifugal stiffening. Additionally, it can handle the offset of the section's centroid relative to the main beam axis. For more detailed information on the numerical implementation of the displacement-based GEBT method, readers can refer to the works of Bauchau [45] and Wang et al. [31].

2.4. Framework of Fluid–Structure Interaction

In this study, the LES wake model, ALM aerodynamic model, and GEBT structural model are divided into three modules. Figure 3 is a flow chart of the aeroelastic model. The LES module solves the Navier–Stokes equations and obtains the flow state Q_n at time T_n. The Actuator Line Model samples the velocity U_n from the module to calculate the aerodynamic loads F_n. The aerodynamic load F_n is then transmitted to the structural module to compute the blade deflection d_n and torsion θ_n.

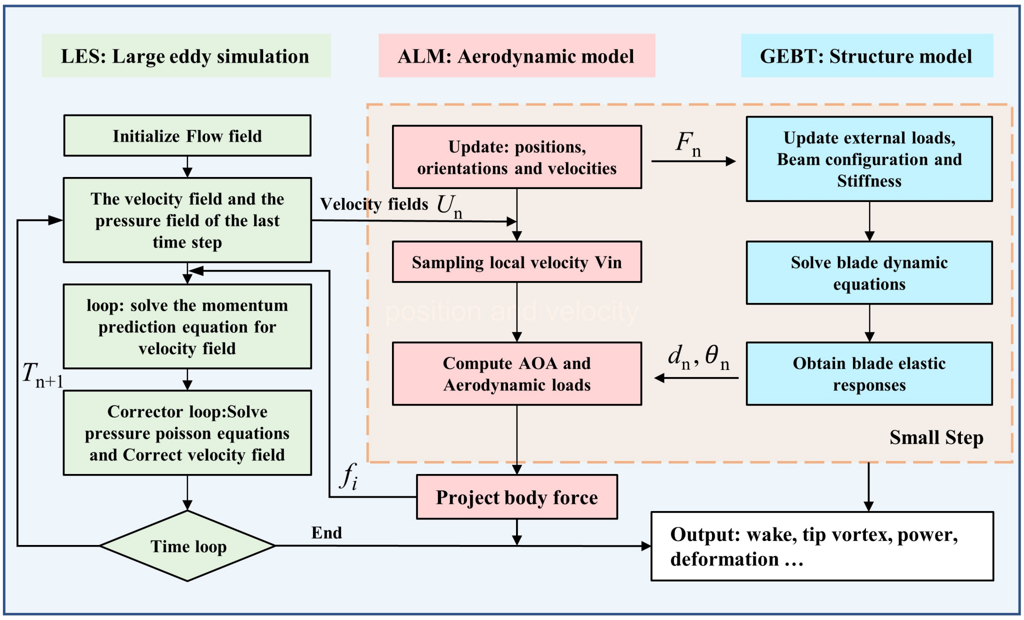

Figure 3. Coupling scheme of the fluid and structural solvers.

Additionally, in this bidirectional fluid–structure coupling model, the deflection velocity associated with d_n is considered when calculating the relative velocity U_{rel} of the blade at time T_n. The blade angle of attack and relative velocity, calculated based on the blade's updated position Equation (4), are used to determine the aerodynamic loads at T_{n+1}. The aerodynamic loads F_{n+1} are then smoothly projected onto the fluid grid using a Gaussian function, and added as a source term f_i to the governing equations; this is used to compute the flow state at time T_{n+1}. At time T_{n+1}, the velocity field on the blades is resampled from this new flow state to compute the aerodynamic loads at that time. Additionally, it is worth noting that the modules are weakly coupled, meaning that each module's variables are computed. Blade deformation and blade forces perform a small time-step calculation loop at each time step [9], to ensure numerical convergence of the structural solver and improve overall computational efficiency.

To avoid numerical oscillations in the simulation due to the chosen time step, the time step for the simulation is constrained using the Courant–Friedrichs–Lewy (CFL) number.

$$CFL_{tip} = \frac{\omega R \Delta t}{\Delta_g} \tag{15}$$

Here, ω is the generator's rotational speed, R is the rotor diameter, and $\Delta_g = \sqrt[3]{\Delta_x \Delta_y \Delta_z}$ is the equivalent element size. The subsequent validation and work in this study are conducted with a time step satisfying the condition $CFL_{\text{tip}} < 1$, as used in previous studies [22,36,46]. In this study, the fluid solver time step is $T_n = 0.015$ s, and the structural subcycle time step is $T_e = 0.0015$ s.

3. Computational Setup

The computational model adopted is the IEA-15MW wind turbine, with a rotor diameter of $D = 240$ m.

3.1. Computational Domain and Mesh

The computational domain is set to a length of 14D. Width and height are 8D. It should be noted that for the IEA-5MW, $D = 120$ m, and for the IEA-15MW, $D = 240$ m. The upstream distance from the wind turbine is set to 4D, downstream to 10D, and the lateral boundaries are at a distance of 4D, to avoid boundary effects and ensure a sufficiently long wake region. Figure 4 provides a detailed description of the grid discretization and boundary conditions in the computational domain, with the turbine location marked in red. The inlet boundary condition is set as uniform velocity inflow, the outlet boundary as zero-gradient, and the bottom, top, and lateral boundaries are set to free-slip conditions. To balance computational accuracy and efficiency, the computational domain is discretized using hexahedral meshes, with four levels of grid refinement, resulting in a finer mesh in the wake region. The finest mesh region extends 5D downstream.

3.2. Sensitivity Analysis

For bidirectional fluid–structure interaction (FSI) using the Actuator Line Model (ALM), substantial user experience is required [47]. Although previous simulation studies based on the NREL-5MW wind turbine have accumulated substantial experience regarding parameters such as projection width [47,48], grid selection, and time step [6,9,43,46,49], significant research experience has been accumulated. However, it remains uncertain whether these experiences are still applicable to modeling of the 15MW wind turbine, which has longer and more flexible blades. Therefore, a sensitivity analysis on projection width ϵ, time step T_n, and grid independence is conducted in this section. It should be noted that the validation and subsequent work in this section do not consider the tower, nacelle, or control system of the IEA-15MW wind turbine.

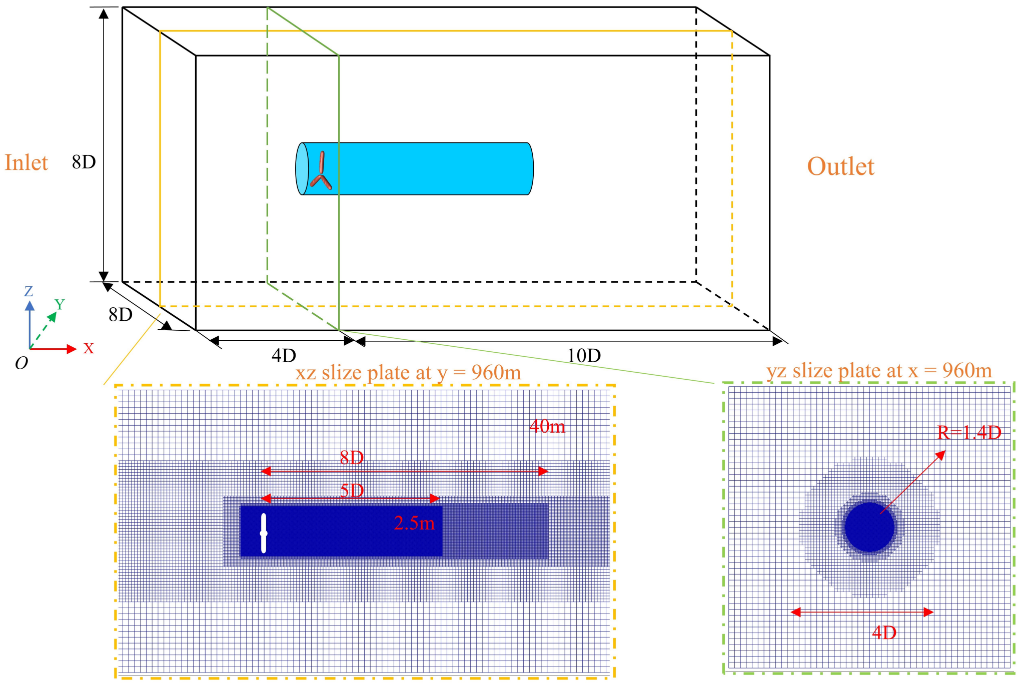

Figure 4. Grid discretization and boundary conditions of the computational domain.

3.2.1. Sensitivity Analysis of Projection Width

A projection width ϵ that is too large can lead to an overestimation of power and thrust, while too small a width may underestimate aerodynamic loads and cause numerical oscillations [41,43]. This will have a profound impact on the wake region. The size of the Gaussian projection width is typically determined based on the grid size [50]. Here, the grid cell size at the rotor is refined to 2.5 m, which is similar to the simulation setup used by Liu [51] and Yang et al. [49]. Projection widths 'ϵ' of 2.5 m (Δ_{grid}), 3.75 m ($1.5 \times \Delta_{\text{grid}}$), 5 m ($2 \times \Delta_{\text{grid}}$), and 6.25 m ($2.5 \times \Delta_{\text{grid}}$) are selected to study in detail the effect of projection size on aeroelastic responses. The simulation is based on an IEA-15MW wind turbine rotating at $\Omega = 7.55$ rpm and a freestream wind speed of $V_0 = 10.59$ m/s.

The data in Table 1 represent the averages over three cycles after the simulation has stabilized. It can be seen that, except for $\epsilon = 2.5$ m, the maximum relative difference between the data of the other three sets is less than 2%, and the values increase as ϵ increases. Figure 5 shows the aeroelastic response under different projection widths. It is observed that smaller values of ϵ lead to significant numerical oscillations in the time-domain responses of rotor thrust and tip deflections, resulting in lower response values. This is because a smaller ϵ concentrates the sampled forces more, reducing the smoothness of the aerodynamic load projection. For larger values of ϵ, the increase in ϵ helps to eliminate numerical singularities in the projection and sampling process [41,48]. The time-domain responses of rotor thrust and tip deflections become smoother, but the response values are overestimated, and due to velocity sampling issues, tip deflection exhibits a top collapse during flap motion [9]. However, the extent of this effect is within an acceptable range. It is worth noting that the choice of projection widths $\epsilon = 3.75$ m, $\epsilon = 5$ m, and $\epsilon = 6.25$ m only has a limited impact on the model accuracy and does not cause significant changes in the aeroelastic response. Considering computational accuracy and response stability, subsequent studies adopt $\epsilon = 5$ m, which corresponds to $2 \times \Delta_{\text{grid}}$, as the standard. Additionally, the relationship between the Gaussian projection width ϵ and the grid, as well as its impact on aerodynamic responses such as rotor thrust and power, has been extensively validated and analyzed by Martínez-Tossas et al. [48] and others. Interested readers can refer to these works for more detailed explanations.

Table 1. Aeroelastic performances with varying body force projection widths (ϵ).

Projection Width (m)	Power (MW)	Thrust (kN)	Flapwise (m)	Edgewise (m)	Torsion (deg)
2.5 (Δ_{grid})	13.49	2297.38	14.13	−1.251	−3.764
3.75 $(1.5 \times \Delta_{\text{grid}})$	14.88	2430.50	14.16	−1.278	−3.768
5 $(2 \times \Delta_{\text{grid}})$	15.07	2445.63	14.10	−1.276	−3.768
6.25 $(2.5 \times \Delta_{\text{grid}})$	15.20	2452.88	14.13	−1.282	−3.766

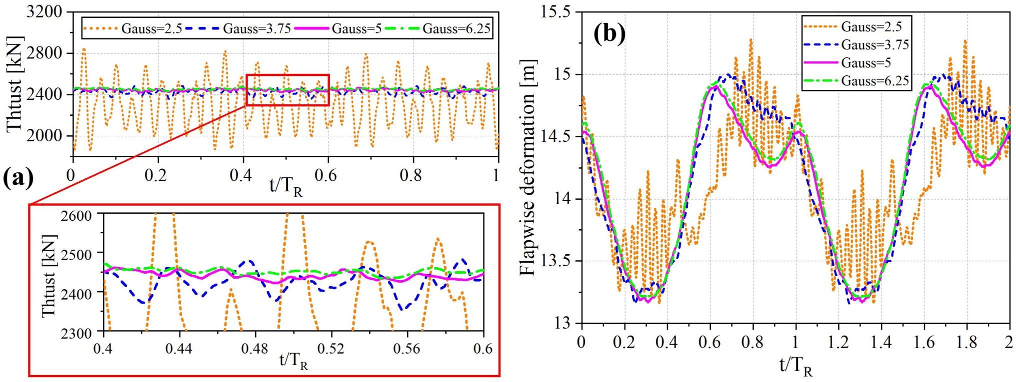

Figure 5. Rotor thrust and flapwise deformation with varying body force projection width (ϵ): (**a**) rotor thrust. (**b**) flapwise deformation. t/T_R represents the ratio of the rotor response time to the rated period, where $T_R = 7.95\,\text{s}$.

3.2.2. Mesh Size Sensitivity Analysis

Under the grid configuration shown in Figure 4, a grid independence study was performed with three grid sets. The grid cell sizes at the rotor were refined to 1.75 m $(2.5/\sqrt{2})$, 2.5 m, and 3.5 m $(2.5 \times \sqrt{2})$, all of which are smaller than the average blade chord length. The total number of grid cells was approximately 5 million, 9 million, and 23 million, respectively. For the coarser grid setup, there are 68 grid cells within the rotor region, with actuator points uniformly distributed along the blade. The spacing between actuator points is $1.5 \times \Delta_{\text{grid}}$ [48,52]. The Gaussian projection width ϵ is determined using the validated criterion $\epsilon = 2 \times \Delta_{\text{grid}}$, which varies with the grid size, ranging from 3.5 m to 7 m. Additionally, under the Courant number criterion Equation (15), the time step T_n will be adjusted as the grid size changes.

The data in Table 2 represent the averages over three cycles after the simulation stabilizes. It can be observed that the differences for all values are within 3%, with response deviations for the coarse and medium grids remaining below 0.5%. In contrast, the maximum error between the fine and medium grids increased to 2.903%, as seen in the thrust numerical response. This is somewhat different from conventional sensitivity analysis, primarily due to the variation in projection width with grid size, leading to numerical instability. Figure 6 shows the dynamic response over three rotor periods for different mesh sizes. As seen in Figure 6a, the refined mesh exhibits larger fluctuations in power and thrust predictions. In contrast, the coarse grid, due to its larger projection width, results in smoother predictions but significantly overestimates the response values. In addition, Figure 6b shows the blade deformation response of different mesh sizes. The fine mesh size shows a better response curve in terms of flapping deformation, although its rotor power and thrust response fluctuate more. This is attributed to the numerical oscillations caused by the smaller projection width ϵ used in the finer grid [48]. In general, the coarse mesh cannot generate tighter tip vortices due to the larger projection width, while the fine mesh underestimates the aerodynamic loads and causes numerical oscillations, and has a higher computational cost. Therefore, considering both computational efficiency and the need for tip vortex identification [53], a medium grid is chosen as the simulation grid for subsequent analyses.

Table 2. Aeroelastic performance under different mesh sizes.

Grid Resolution	Thrust (kN)	Error (%)	Power (MW)	Error (%)	Flapwise (m)	Error (%)
Coarse	2438	-	14.54	-	13.86	-
Medium	2425	0.433	14.47	0.482	13.81	0.361
Fine	2386	1.608	14.05	2.903	13.92	0.767

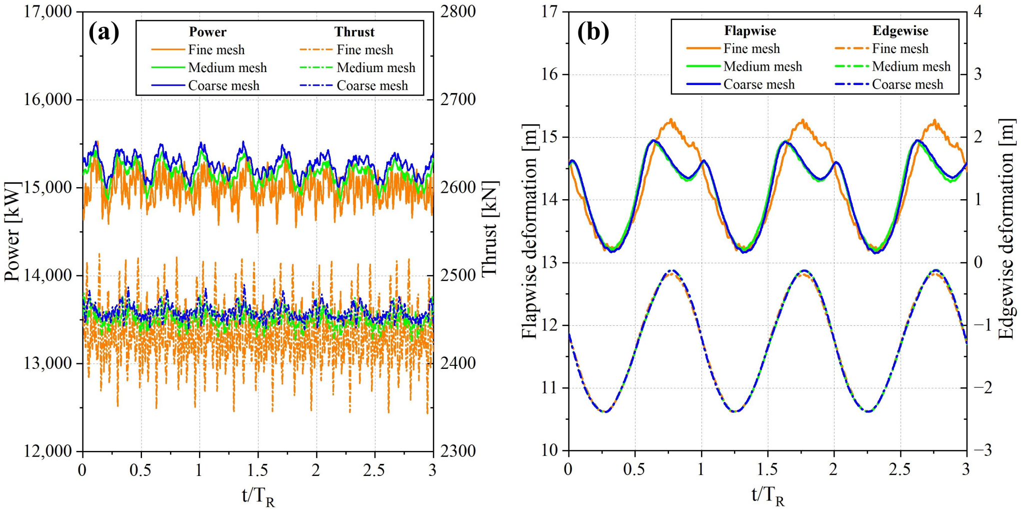

Figure 6. Aeroelastic response under different mesh sizes: (**a**) rotor power and thrust; (**b**) flapwise and edgewise deformation.

4. Results and Discussion

4.1. Aeroelastic Model Validation

Table 3 shows the characteristics of the NREL-5MW and IEA-15MW wind turbines. It can be seen that their rotor radii are 61.5 m and 117 m, respectively, indicating that the 15MW wind turbine has more slender blades, making it more susceptible to larger geometric nonlinear deformations. Most of the current aeroelastic work on wind turbines is based on the NREL-5MW model, with a wealth of test and simulation results from various aeroelastic models. Therefore, the validation work in this section first verifies the reliability of the method is validated by comparing it with simulations of NREL-5MW using different aeroelastic models. Then, the accuracy of this nonlinear aeroelastic model in handling large flexible deformations of the blade is validated by comparing simulations of the IEA-15MW with OpenFAST-3.5.0

Table 3. The properties for NREL-5MW and IEA-15MW wind turbines.

Parameter	NREL-5MW	IEA-15MW
Blade length	61.5 m	117 m
Blade prebend	-	4 m
Cut-in, rated, cut-out wind speed	3 m/s, 11.4 m/s, 25 m/s	3 m/s, 10.59 m/s, 25 m/s
Cut-in, rated rotor speed	6.9 rpm, 12.1 rpm	5.0 rpm, 7.55 rpm
Overhang, shaft tilt, precone angle	5 m, 5 degrees, 2.5 degrees	11.35 m, 6 degrees, −4 degrees

4.1.1. 5MW Model Verification

In this section, the aeroelastic model proposed in this study is validated by simulating the FSI of the NREL-5MW wind turbine model. NREL-5MW is a generic wind turbine model widely used for the validation of turbine elasticity and wake simulations [6,8,24,34]. We have summarized some classic aeroelastic coupling methods and recent works, and performed a comparative analysis with the simulation results of this study. These include the isotropic ALM nonlinear beam model (ALFBM) [35], the anisotropic projection combined with multibody dynamics (ALM-GEBT) [9], the Actuator Curve Embedding Model coupled with the nonlinear beam method (ACE-FEM) [49], the isotropic projection ALM coupled with the nonlinear beam method [36], the fully analytical coupling method (CFD-CSD) [8], the CFD coupled with the geometrically exact beam method (CFD-GEBT) [34], the reference BEM-GEBT (OpenFAST) [40] and the official NREL report [54].

To evaluate different methods, the base grid size used for validation is 32 m, with four levels of grid refinement. The finest grid size Δ_{grid} in the rotor region is 2 m, following the criterion $\epsilon = 2\Delta_{\mathrm{grid}}$. The uniform Gaussian projection width 'ϵ' is set to 4 m, which has been widely used in the works of Huang et al. [36], Ma et al. [35], and Yang et al. [49].

Table 4 shows that the different methods exhibit high consistency in predicting rotor power, flapwise deflection, and edgewise deflection. However, there are relatively greater discrepancies in rotor thrust and blade tip torsion. Overall, the differences in the response data are not large and remain within the same order of magnitude. This indicates that all methods are able to reasonably predict the aeroelastic performance of wind turbines. Specifically, rotor power and thrust values obtained from full-resolution CFD simulation methods such as Dose et al. [8] and Honing et al. [34] are generally higher than those from other methods. This may be due to the introduction of empirical loss correction models in aerodynamic models such as ALM and BEM. Although this method shows some overestimation in rotor power compared to other ALM models, it is more in line with CFD model results, but the differences are not significant, and the overall values are closer to the results of mature commercial software such as OpenFAST. It is worth mentioning that previous studies [48] have pointed out that ALM models typically require a trade-off between rotor power and thrust in calculations, and when the simulated results are closer to the true power, the accuracy of thrust may decrease. Therefore, balancing rotor power and thrust is crucial. Furthermore, differences in computational settings (such as tower tilt angle, hub effects, tower deformation, and gravitational loads) among different methods can influence the simulation results. Overall, the simulation results obtained using the current method are in good agreement with the reference data, especially when compared to the simulation results from OpenFAST, showing higher similarity, which demonstrates the accuracy of the proposed aeroelastic model. Finally, the linear Euler–Bernoulli beam model is reasonable for simulating a 5 MW wind turbine under rated conditions, a conclusion also supported by Muscari et al. [39] and Yang et al. [49].

Additionally, a detailed comparison of the tip deflections within the rotor cycle was conducted for several methods: OpenFAST [40], CFD-CSD [8], ALM-GEBT [9], and ACE-FEM [49]. Since the convergence conditions vary between the models, a comparison was made using one cycle of data at the respective converged conditions for each method. Figure 7 shows that all methods effectively simulate the periodicity of rotor deformations and produce similar numerical results. The spanwise distributions of flapwise and edgewise deformations predicted by each method demonstrate consistency, as seen in Figure 8. However, in the prediction of torsional deformations, discrepancies are observed near the blade tips across models, primarily due to differences in structural models and the definition of torsional directions. Nevertheless, this method shows a high level of similarity in prediction results compared to methods like OpenFAST. This indicates that the structural model of this method accurately predicts structural deformations, thereby validating the accuracy of the proposed aeroelastic model. Additionally, compared to flapwise and edgewise deformations, the torsional deformation of the NREL-5MW wind turbine is numerically negligible. Sun [55] also noted that the bending–torsion coupling nonlinearity in the NREL-5MW wind turbine is not significant.

Table 4. Aerodynamic performance and blade tip deflection of NREL 5MW wind turbine at rated wind speed.

Study	Power (MW)	Thrust (kN)	Flapwise (m)	Edgewise (m)	Torsion (deg)
BEM-Model (NREL) [54]	5.28	814.45	5.47	−0.61	-
CFD-CSD (Dose et al., 2018) [8]	5.49	769.40	5.55	−0.62	0.29
ALFBM (Ma et al., 2019) [35]	5.35	663.00	6.21	−0.58	-
ALM-GEBT (Leng et al., 2023) [9]	5.26	728.50	5.53	−0.55	−0.12
ALM-beam (Huang et al., 2024) [36]	5.23	658.48	4.50	−0.57	2.96
CFD-GEBT (Höning et al., 2024) [34]	5.43	759.20	5.51	−0.60	−0.45
ACE+FEM (Yang et al., 2024) [49]	5.25	714.53	5.70	−0.59	0.10
BEM-GEBT (OpenFAST) [40]	5.29	724.60	5.42	−0.60	−0.12
Present	5.43	725.50	5.45	−0.62	−0.12

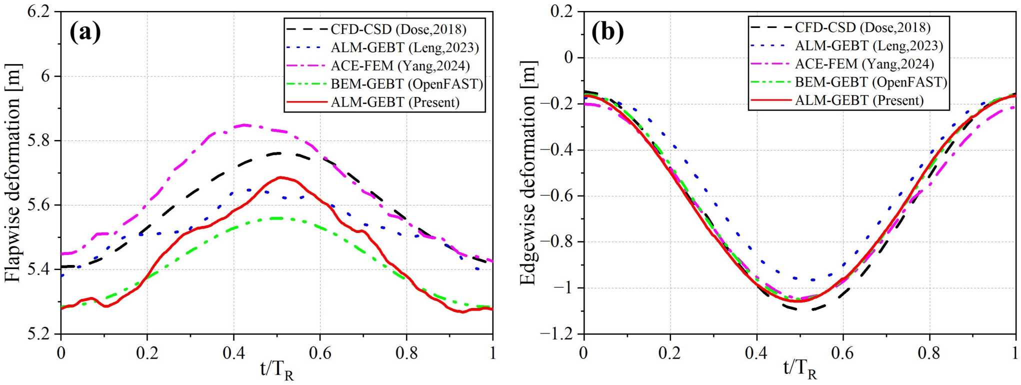

Figure 7. The periodic deflection of the tip at rated wind speed for 5MW: (**a**) flapwise deformation. (**b**) Edgewise deformation. CFD-CSD (Dose , 2018) [8]; ALM-GEBT (Leng , 2023) [9]; ACE+FEM (Yang , 2024) [49].

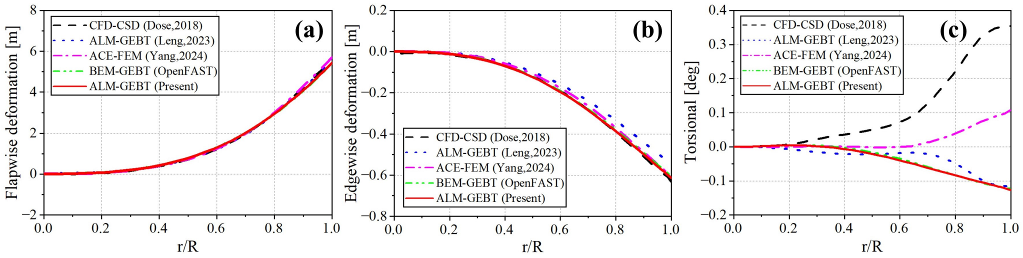

Figure 8. Distribution of blade deflection along the blade at rated wind speed for 5MW: (**a**) Flapwise deformation. (**b**) Edgewise deformation. (**c**) Torsional deformation. r/R represents the ratio of the blade position to the total blade length, where $R = 117$ m. CFD-CSD (Dose , 2018) [8]; ALM-GEBT (Leng , 2023) [9]; ACE+FEM (Yang , 2024) [49].

4.1.2. 15MW Model Verification

This section validates the reliability and accuracy of the proposed model for large wind turbines with significant nonlinear effects by comparing it with OpenFAST. The computational model used is the IEA-15MW wind turbine, which features 120 m long blades with pronounced bending–torsion coupling nonlinear characteristics [10,30,55].

As shown in Table 5, under rated operating conditions, this method demonstrates high consistency in predicting rotor power, rotor thrust, and blade tip torsion. Similar results are also observed for flapwise and edgewise deformations, with relative mean errors of 3.688% and 3.718%, respectively. This indicates that the current model can predict the average performance of wind turbines with reasonable accuracy.

Table 5. Aeroelastic performance of the IEA 15MW wind turbine at rated wind speed.

Model	Power (MW)	Thrust (kN)	Flapwise (m)	Edgewise (m)	Torsion (deg)
OpenFAST	15.21	2445.8	14.64	−1.3257	−3.752
Present	15.07	2441.5	14.10	−1.2664	−3.768

The tip deformation responses over five rotor cycles, as shown in Figure 9, reveal that this method and OpenFAST exhibit similar in-plane and out-of-plane response trends. This method and OpenFAST share identical periodic trends in in-plane and out-of-plane responses. Compared to OpenFAST, this method exhibits nearly twice the fluctuation amplitude in flapwise deformation response, primarily due to a lower lower-bound response. Additionally, there is a tip response collapse caused by velocity fluctuations in the flow field and the Gaussian projection model. It is important to emphasize that the numerical differences between the two are minimal and do not significantly impact the simulation results. Both methods show the same trend in edgewise deformation, with a maximum peak response error of less than 0.05 m. For torsional deformation, this method aligns well with the reference data in both numerical values and response trends.

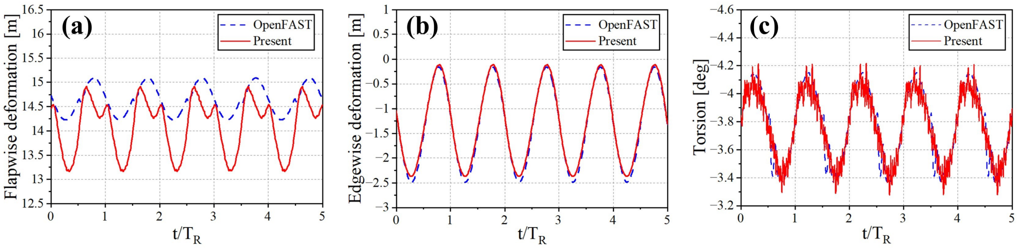

Figure 9. Tip deflection of the 15MW wind turbine at rated wind speed: (**a**) Flapwise deformation. (**b**) Edgewise deformation. (**c**) Torsional deformation.

Figure 10 demonstrates that this method accurately predicts the spanwise distribution of blade deformations in the flapwise, edgewise, and torsional modes, with minimal error. Additionally, The coupling method has a smaller impact on blade edgewise deformation, which is consistent with the research conclusions of Della Posta et al. [4] and Santoni et al. [37]. Overall, the results obtained by this method are in excellent agreement with the reference results, demonstrating that the current model can accurately simulate the aeroelastic responses of flexible blades with significant bending–torsion coupling nonlinear effects.

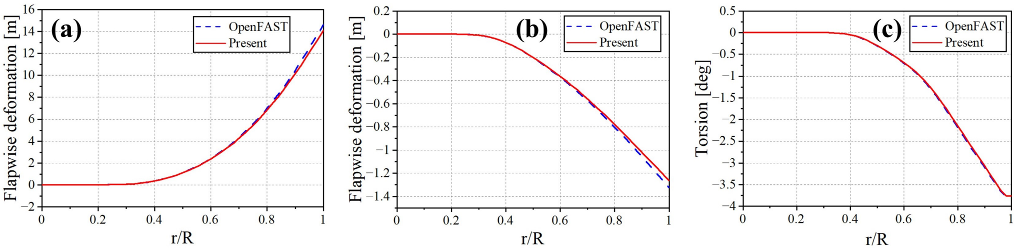

Figure 10. Distribution of blade deflection along the blade at rated wind speed for 15MW: (**a**) Flapwise deformation. (**b**) Edgewise deformation. (**c**) Torsional deformation.

4.2. Aeroelastic Response Under Different Structural Models

We applied the proposed nonlinear model and a linear model based on the Euler–Bernoulli beam theory to simulate the IEA-15MW wind turbine. We further investigated the effects of geometric nonlinearities in large flexible blades on aerodynamic loads, blade deformations, and wake characteristics. It should be emphasized that EALM refers to the linear aeroelastic model using the Euler–Bernoulli beam structure, while GALM refers to the nonlinear aeroelastic model based on the Geometrically Exact Beam Theory. Apart from differences in the structural models, all other computational settings remain identical for both methods.

4.2.1. Aerodynamic Load Comparison Analysis

The comparative analysis of the two models was conducted over three stabilized rotor cycles after 600 s of numerical simulation, eliminating the effects of initial transient behavior. Figure 11 shows the power and thrust coefficient responses over three rotor cycles under different models. The results indicate that rotor power and thrust are significantly affected by nonlinear effects, decreasing by 6.98% and 12.73%, respectively. The impact of nonlinear deformation on rotor thrust is approximately twice that on rotor power. Additionally, the linear model performs poorly in predicting the thrust response trend, exhibiting collapses in extreme regions, multiple peaks, and an increase in oscillation amplitude by 69.56%. This suggests that for large flexible-blade wind turbines with blade lengths exceeding 100 m, the Euler–Bernoulli beam should be used with caution for simulations. It should be noted that the nonlinear model exhibits more high-frequency noise in the thrust and power responses, which is likely due to the geometrically exact beam model requiring smaller time steps to ensure convergence. However, these noise points have little impact on the overall response trends and numerical results.

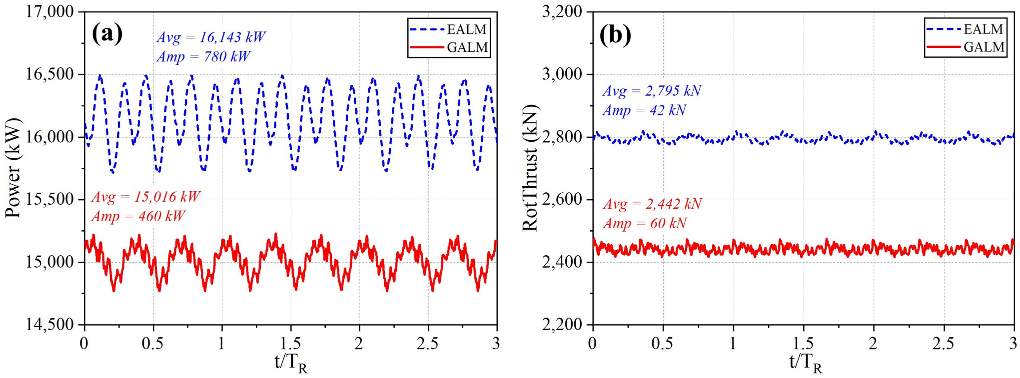

Figure 11. Comparative analysis of aerodynamic loads for EALM and GALM at rated wind speed: (**a**) Aerodynamic power. (**b**) Aerodynamic thrust.

To further investigate the reasons behind the differences in rotor thrust and rotor power between different structural models, a comparative analysis of numerical responses such as AOA and U_{mag} at each aerodynamic calculation point along the blade was conducted. Figure 12 shows the difference in AOA responses between the two models. It can be observed that differences begin to appear beyond the spanwise location of 0.4 r/R, with GALM predicting a lower AOA. This difference increases with the spanwise distance, reaching approximately 4° at the blade tip. According to Equation (4), this implies that the nonlinear model predicts lower aerodynamic forces on the blade, which is further validated in subsequent analyses. Figure 13 shows the difference in (U_{mag}) responses between the two models. It can be observed that the linear model shows only a slight increase and does not exhibit significant differences like AOA. The transient responses in the spatiotemporal distributions remain consistent between the two models. It is noteworthy that both models exhibit periodic spatiotemporal distributions of AOA and U_{mag}, with consistent regions and trends of variation. Additionally, the sharp variations in angle of attack (AOA) observed between 0.9 and 1.0 r/R are likely caused by the use of the tip loss function.

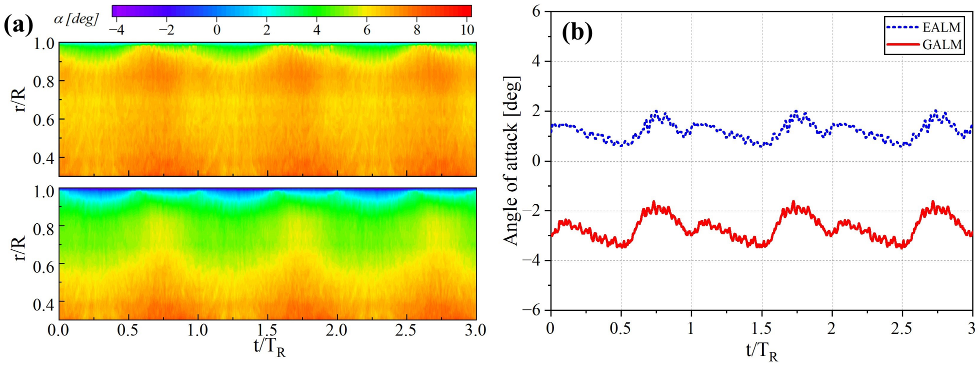

Figure 12. Angle of attack (AOA) for EALM and GALM at rated wind speed: (**a**) Variation in the blade spanwise distribution. (**b**) Blade tip response.

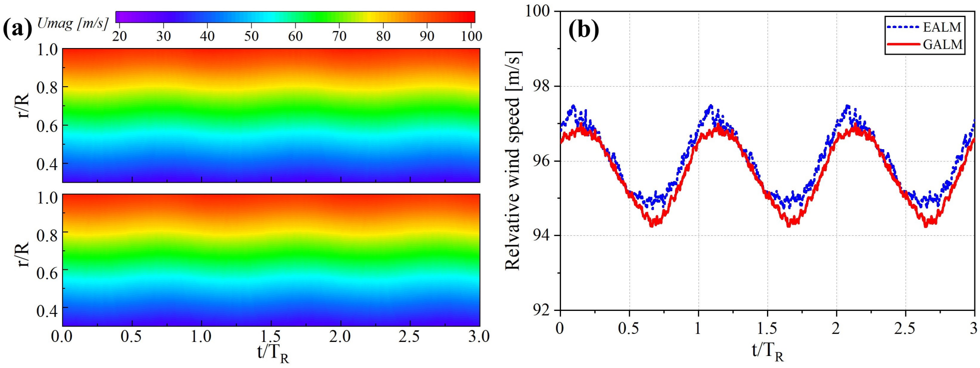

Figure 13. Relative speed (U_{mag}) for EALM and GALM at rated wind speed: (**a**) Variation in the blade spanwise distribution. (**b**) Blade tip response.

The distributions of AOA and (U_{mag}) on the blade are shown in Figure 14. The (U_{mag}) predictions of the two models tend to agree, with significant differences primarily observed in AOA. These differences are more pronounced near the blade tip. This discrepancy arises from differences in the properties of the structural models, as the linear model EALM does not account for blade torsional deformation. In large flexible blades, stronger torsional characteristics are evident, and these effects are further amplified in the nonlinear model. This amplification leads to significant differences in AOA predictions.

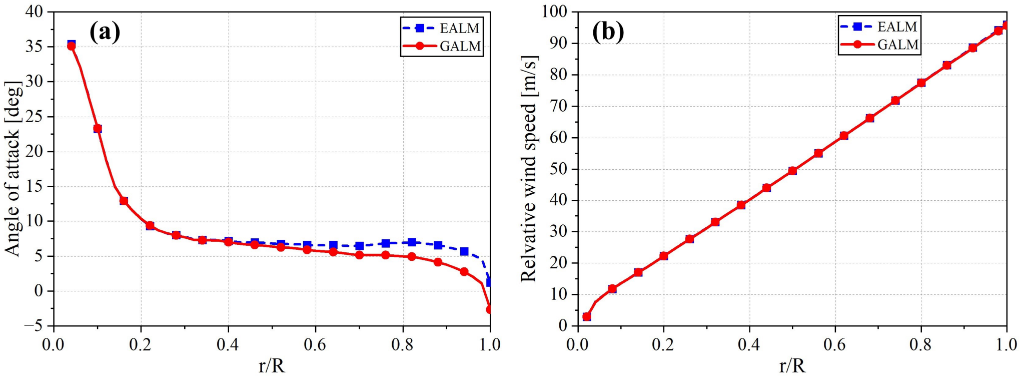

Figure 14. Distribution of angle of attack (AOA) and relative speed (U_{mag}) along the blade for EALM and GALM at rated wind speed: (**a**) AOA. (**b**) U_{mag}.

These differences in AOA can significantly affect the predicted results of the blade aerodynamic loads. Figure 15 shows the spanwise distribution of the blade tangential and axial forces. As reflected by the differences in AOA, discrepancies in axial and tangential forces between the two models also begin at a spanwise location of 0.4 r/R, and gradually increase along the span. The maximum difference is observed at a spanwise location of 0.85 r/R. This is due to the combined effects of the blade characteristics, bending–torsion coupling deformation, and tip loss function in the middle and rear sections of the blade. The axial and tangential forces predicted by the linear model EALM are both higher. The differences are particularly pronounced in the tangential force, with local tangential force discrepancies reaching approximately 70%. This difference explains the source of the disparity in thrust and power between the models. It is evident that for the aeroelastic responses of large flexible blades, the linear beam model exhibits deficiencies in both overall aerodynamic performance and local aerodynamic force predictions. Geometric nonlinear effects should not be neglected in the aeroelastic simulations of large flexible blades.

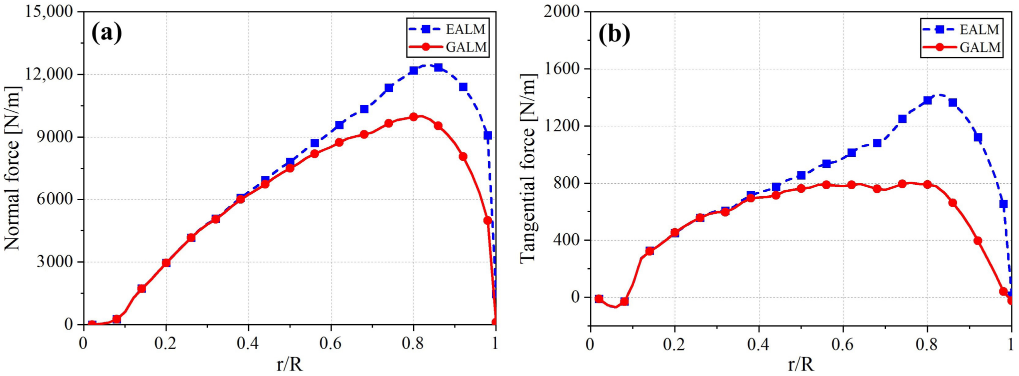

Figure 15. Distribution of aerodynamic loads along the blade for EALM and GALM at rated wind speed: (**a**) Normal force. (**b**) Tangential force.

4.2.2. Blade Deformation Comparison Analysis

In order to further explore the effect of aerodynamic differences on blade deformation, a comparative analysis of parameters such as flapwise deformation, edgewise deformation, and torsion was conducted. Three cycles under stable operating conditions were selected for transient comparison. Figures 16 and 17 illustrate the spatiotemporal distributions of blade flapwise and edgewise deformations under different models. Both models exhibit similar periodic trends, but the nonlinear model predicts smaller flapwise and edgewise deformations than the linear model. The linear model EALM predicts a tip flapwise displacement of 15.920 m and an edgewise displacement of −0.685 m. In contrast, the nonlinear model GALM predicts a tip flapwise displacement of 14.10 m and an edgewise displacement of −1.2714 m. This indicates that the linear model EALM overestimates tip flapwise deformation by 12.91% and tip edgewise deformation by 46.13%. The impact of nonlinear effects is more pronounced for edgewise deformation. Additionally, the nonlinear model GALM exhibits larger extreme oscillations in out-of-plane tip deflection, reflecting its capability to capture the characteristics of geometric nonlinear deformation.

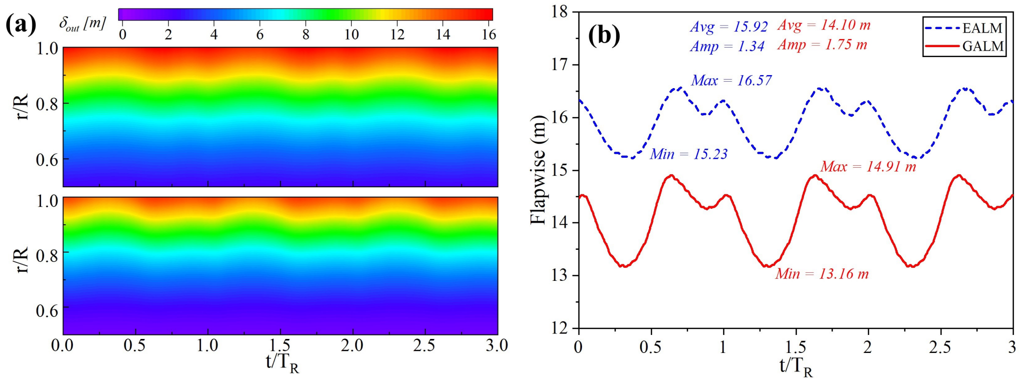

Figure 16. Flapwise deformation for EALM and GALM at rated wind speed: (**a**) Variation in the blade spanwise distribution. (**b**) Blade tip response.

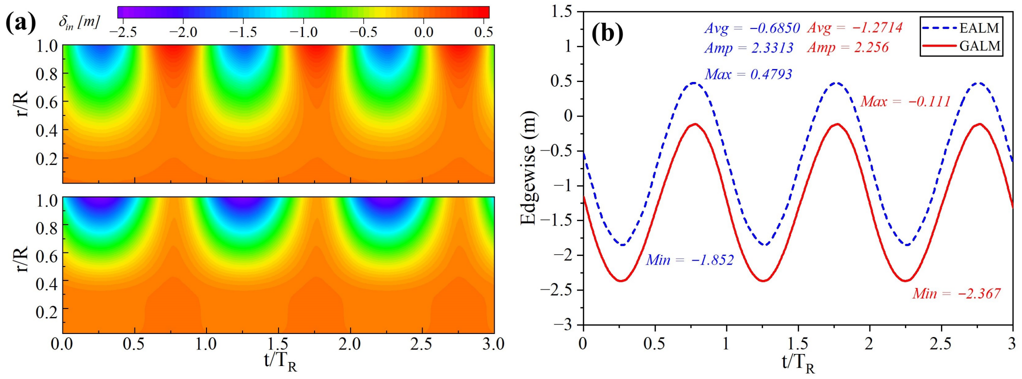

Figure 17. Edgewise deformation for EALM and GALM at rated wind speed: (**a**) Variation in the blade spanwise distribution. (**b**) Blade tip response.

Figure 18 shows that the torsional distribution of the nonlinear blade exhibits a clear periodic trend, with tip torsion oscillating between $-4.1° \sim -3.3°$. According to Equation (6), this torsion significantly reduces the blade's angle of attack (AOA), thereby decreasing the aerodynamic loads. This change in loads further impacts blade deformation.

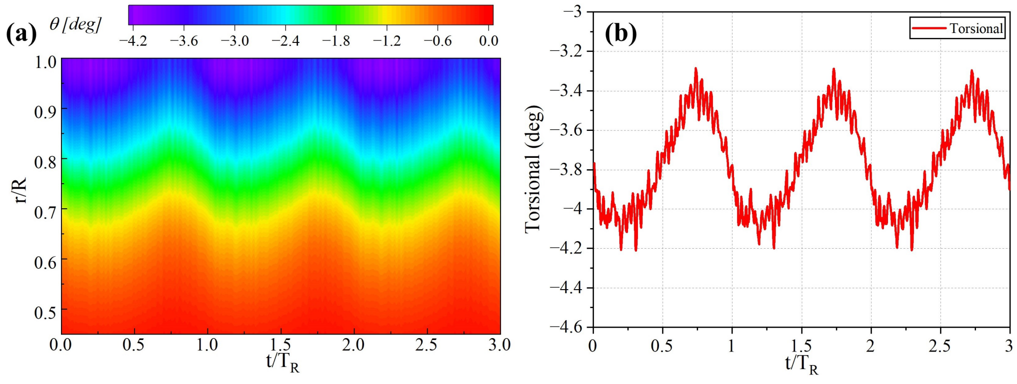

Figure 18. Torsional deformation for EALM and GALM at rated wind speed: (**a**) Variation in the blade spanwise distribution. (**b**) Blade tip response.

Figure 19 illustrates the spanwise distributions of blade flapwise deformation, edgewise deformation, and torsion. Firstly, for flapwise deformation, both models exhibit similar trends, but the deformation predicted by the nonlinear model is overall smaller than that of the linear model. Additionally, the onset of variation is closer to the blade tip, with significant differences observed between the blade midsection and tip, highlighting more pronounced nonlinear characteristics. Secondly, although the linear model predicts the onset of edgewise deformation at an earlier position, its tip edgewise deformation magnitude is smaller. This makes it difficult to accurately capture the nonlinear characteristics of edgewise deformation. Evidently, due to the nonlinear effects of large flexible blades, the linear model performs poorly in predicting the geometric nonlinear characteristics of the blade. In contrast, the nonlinear model better captures the geometric nonlinear characteristics of edgewise deformation. Furthermore, the strong nonlinearity between bending and torsion results in more pronounced differences between the two models when predicting the edgewise deformation of the blade. Finally, the nonlinear model accurately captures the geometric nonlinear torsional deformation of large flexible blades. Torsion begins at a spanwise location of 0.4 r/R and gradually increases towards the blade tip. This corresponds to the location where the AOA differences between the two models begin. This indicates that torsion is the fundamental cause of the discrepancies in aerodynamic performance predictions between the two models.

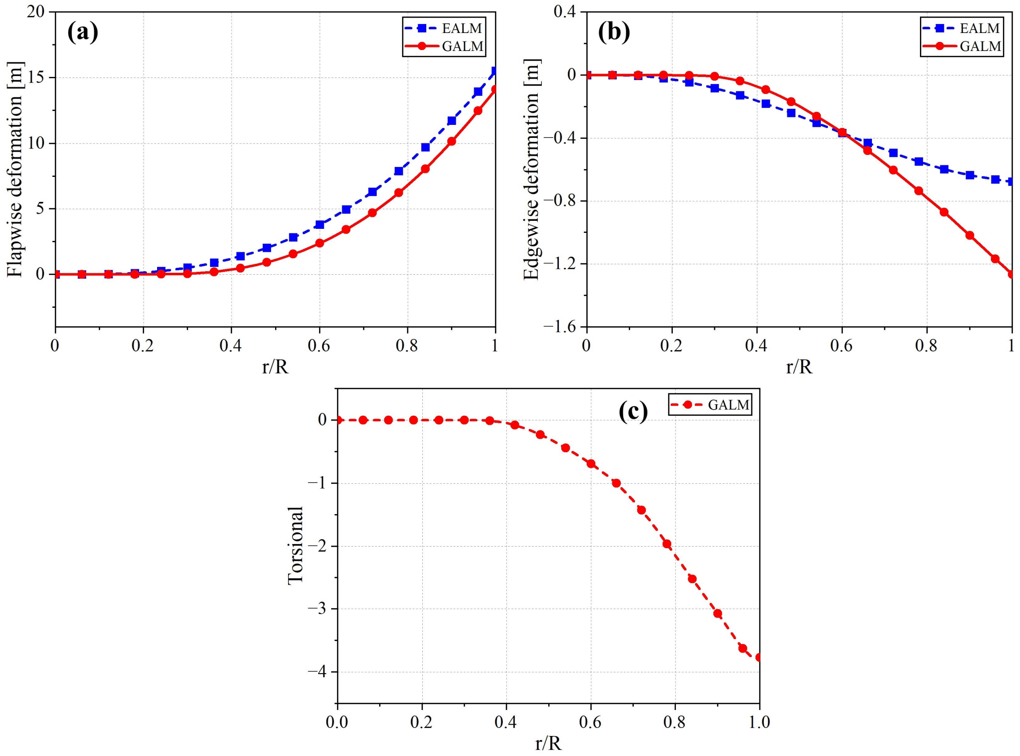

Figure 19. Distribution of blade deformation along the blade at rated wind speed for EALM and GALM: (**a**) Flapwise deformation. (**b**) Edgewise deformation. (**c**) Torsional deformation.

4.2.3. Wake Characteristic Analysis

This subsection compares and analyzes the flow field simulation results of different structural models. Significant differences are observed between the nonlinear model GALM and the linear model EALM in terms of thrust coefficient, blade load distribution, and tip displacement. These differences impact the wake characteristics, including tip vortex strength, average wake velocity, and turbulence intensity.

Figure 20 shows the instantaneous vortex structures at 650 s (about 81.76 blade rotation cycles), colored by the average velocity U_{avg}, illustrating the tip vortices and root vortices under the two structural models. It can be observed that, compared to the linear model EALM, the nonlinear model GALM exhibits smoother load variations near the blade tip (Figure 15). This significantly reduces the tip vortex strength, making the tip vortex structures more prone to dissipation, thereby slowing the merging and breakup of vortex structures. As a result, the nonlinear model generates fewer wake structures in the far-wake region.

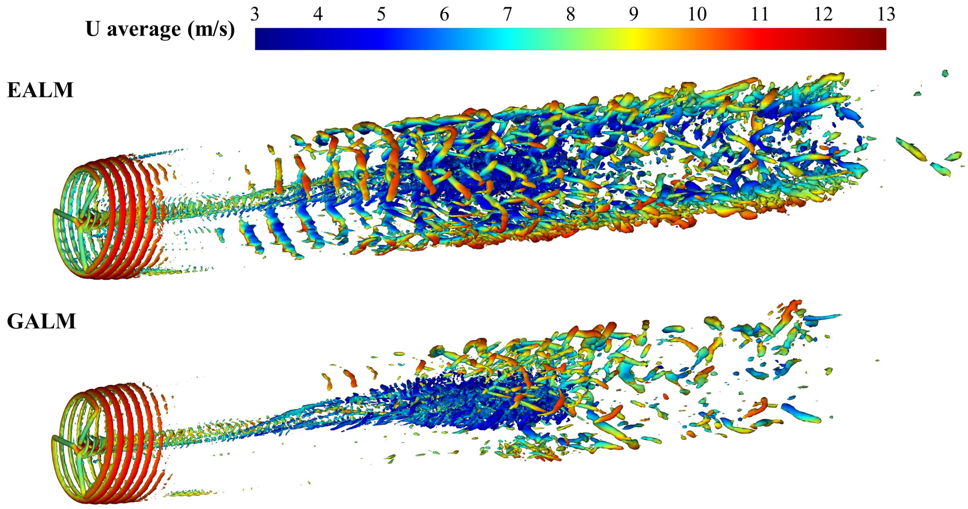

Figure 20. Vortex structure (Q = 0.001) at rated wind speed for EALM and GALM.

Figure 21 shows the Q-criterion slice at the hub height in the XY plane. Compared to the linear model EALM, the nonlinear model GALM exhibits significantly lower tip vortex and root vortex intensities. This is primarily attributed to the smaller force load gradients near the blade tip region. This difference intensifies as the wake develops downstream and becomes more pronounced in the far wake. The linear model EALM generates more chaotic vortices, which may enhance energy and momentum exchange between the tip vortex and the central vortex region, thereby accelerating wake recovery. In contrast, the nonlinear model GALM better preserves the integrity of its tip vortices. Additionally, the discontinuities in the tip vortices and root vortices observed in some regions may be caused by grid refinement. Overall, differences in structural models significantly affect the wake field of a wind turbine. The following sections will delve deeper into how these differences affect the average wake velocity and turbulence intensity profiles.

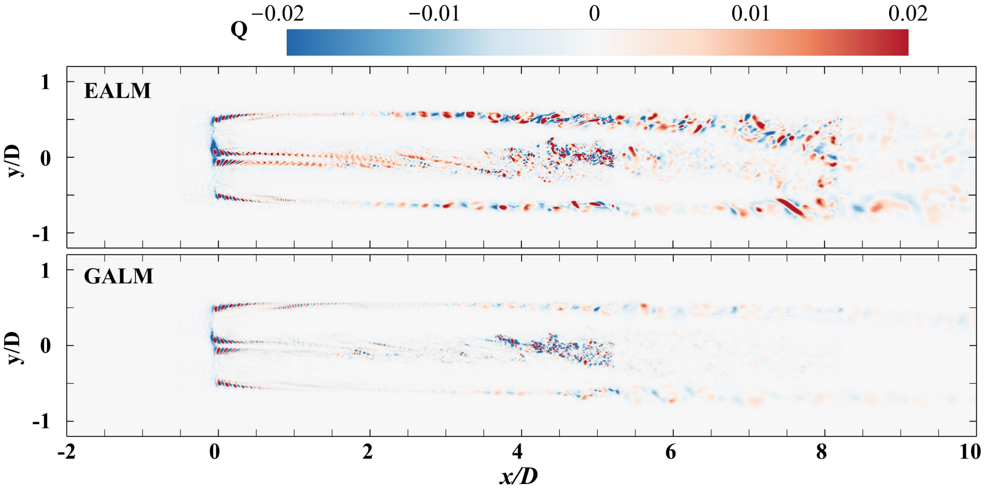

Figure 21. Comparative analysis of vortex structure contours at hub-height horizontal plane (z = 0 m) for EALM and GALM.

Figure 22 presents a comparison of the time-averaged velocity field in the horizontal and vertical planes at the rotor center. The time-averaging range spans three rotor cycles (24 s) after 650 s. In the near-wake region (<4D), the streamwise velocity in the wake is higher for the nonlinear model GALM, primarily because the nonlinear deformation of the blades leads to a significant reduction in the energy extracted by the rotor from the wind. This can be observed in the previously discussed variations in thrust coefficients for the two models (Figure 11). However, as the wake develops, GALM exhibits lower streamwise velocities in the far-wake region, with relatively smoother wake region variations. In contrast, EALM shows more pronounced turbulent behavior. This indicates that in the nonlinear model, the mixing between the low-speed wake and the high-speed ambient flow occurs more slowly and with less intensity. This is caused by the weaker vortex energy and momentum exchange in the far-wake region for GALM (Figure 21). Additionally, both models exhibit downward and upward shifts in the wake center. This is attributed to the rotor shaft tilt angle and the rotor's rotational direction of the wind turbine.

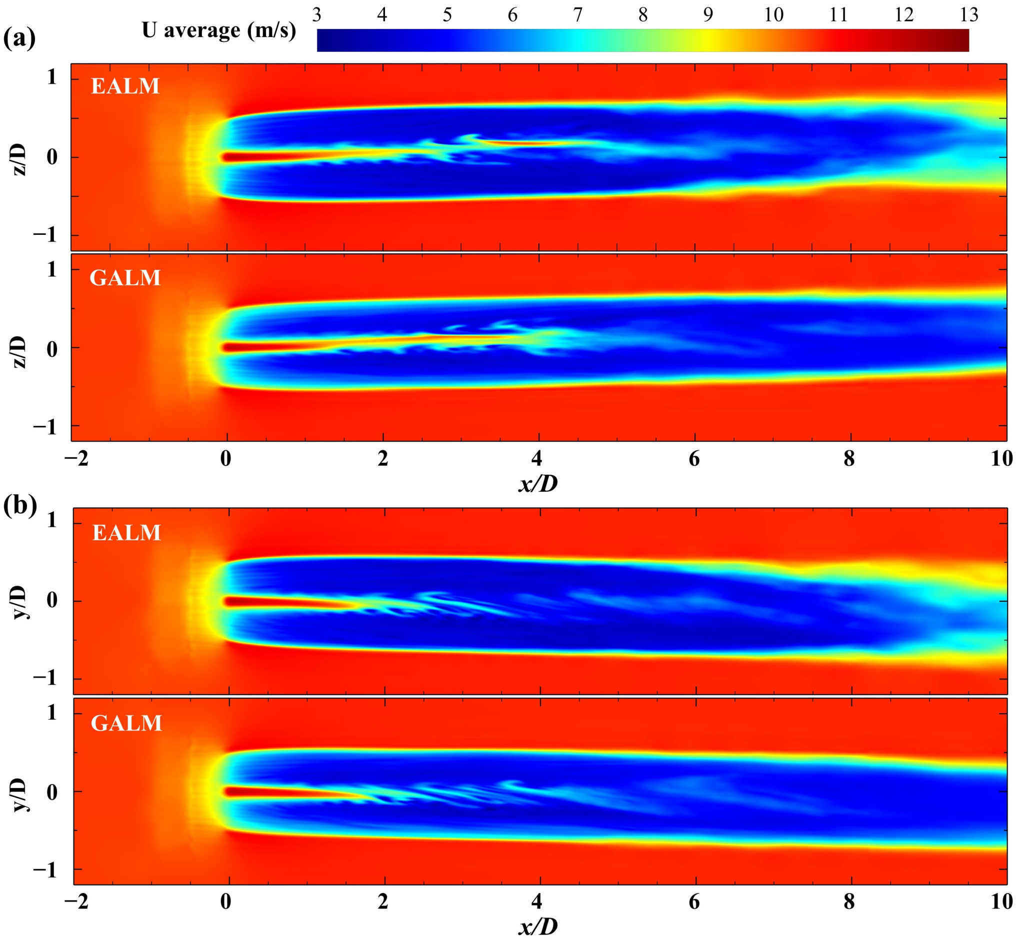

Figure 22. The wake-averaged velocity field in EALM and GALM: (**a**) In the vertical plane (y = 0 m). (**b**) In the horizontal plane (z = 0 m). x/D represents the ratio of the flow field position to the wind turbine diameter, where $D = 240\,\mathrm{m}$.

Figure 23 shows the distribution of time-averaged wake velocity for EALM and GALM. In (Figure 23a), the cross-section is taken at 2D intervals along the flow direction. (Figure 23b) depicts the time-averaged velocity deficit curves plotted for each cross-section. Further downstream, it can be seen that the high-turbulence kinetic energy (TKE) region generated by the tip shear layer gradually mixes with the flow near the wake centerline. Compared to GALM, EALM exhibits earlier and more intense mixing of these regions, indicating that wake velocity recovery occurs earlier and faster in the far-wake region. The offset and expansion of the rotor wake region are also observed. Additionally, EALM exhibits a broader velocity profile and a higher recovery rate, particularly in the recovery of the rotor edge region. Significant differences are also observed in the velocity deficit distribution regions between the two models. The largest discrepancy occurs at the rotor tip, with noticeable differences starting from 4D downstream. This may be attributed to differences in the aerodynamic forces acting on the blades.

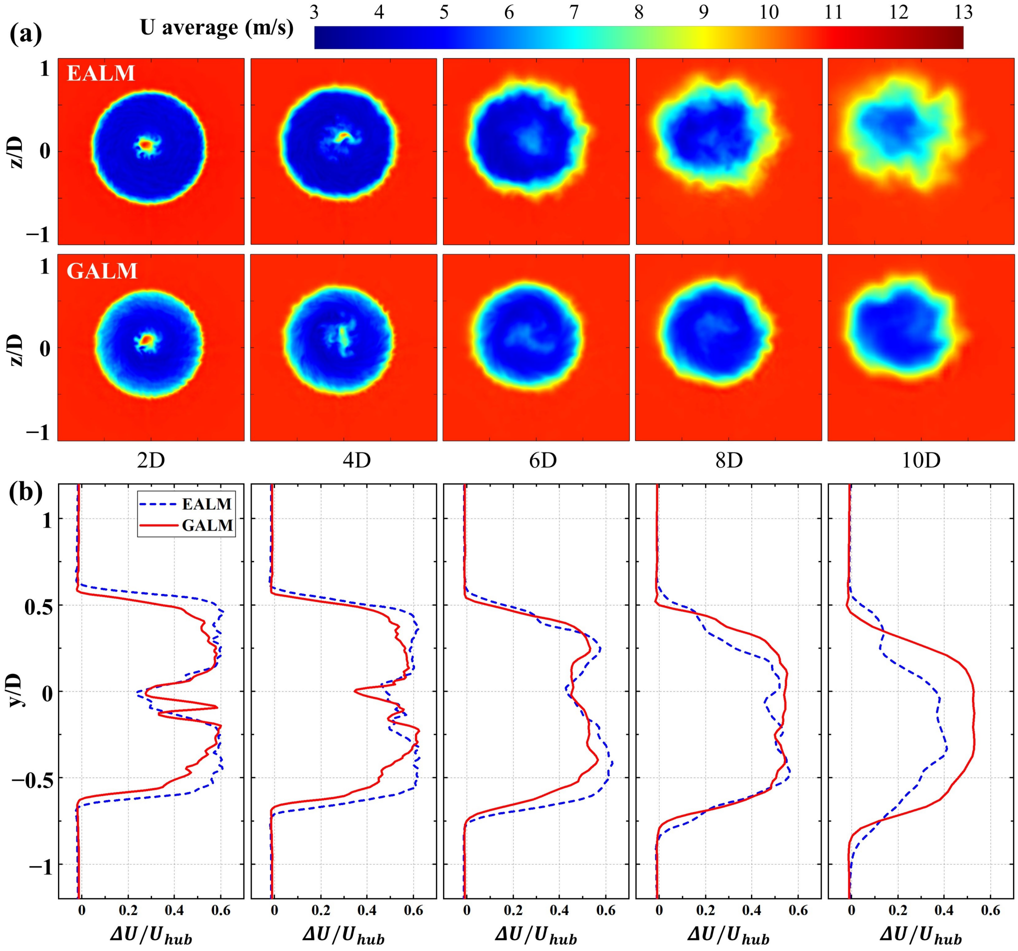

Figure 23. The wake-averaged velocity field in EALM and GALM: (**a**) The average velocity contour. (**b**) The streamwise velocity deficit profiles at hub height (z = 0 m). $\Delta U/U_{\text{hub}}$ is a dimensionless parameter that reflects the wake velocity loss, $\Delta U = U_{\text{hub}} - U_{\text{mag}}$, $U_{\text{hub}} = 10.59\,\text{m}$.

In the 2D position of Figure 23b, both the spanwise wake axial velocity deficit distribution and aerodynamic load distribution (Figure 15) begin to show differences near the 0.5 r/R position. This may be the primary source of the wake differences between the two models. Compared to the nonlinear model GALM, the linear model EALM exhibits more pronounced velocity deficits at the tip region. As the wake develops, the velocity deficit gradually decreases, with the recovery rate being fastest in the tip region and progressively extending toward the wake centerline. At the 8D position, the velocity deficit in the rotor wake region of EALM is already smaller than that of GALM, and this difference becomes further pronounced at the 10D position. This indicates that EALM begins significant wake recovery before the 6D position, while GALM shows delayed recovery with a lower recovery rate. It can be seen that neglecting geometric nonlinear effects may lead to an overestimation of far-field wake recovery rates.

In addition, the turbulence intensity is compared to further study the difference in wake performance caused by the two different structural models, especially in the far-wake region. The turbulence intensity is calculated by

$$I = \sqrt{\frac{1}{3U_{hub}^2}(u'^2 + v'^2 + w'^2)} \tag{16}$$

where u', v' and w' stand for the fluctuating velocity components, and U_{hub} is the inflow velocity of 10.59 m/s in this paper.

As shown in Figure 24a, the linear model exhibits higher turbulence intensity in both the near- and far-wake regions. Specifically, in the far-wake rotor tip region, the turbulence intensity and diffusion range increase significantly. In contrast, the nonlinear model shows a turbulence distribution in the far-wake region that is similar to the near wake, with less variation.

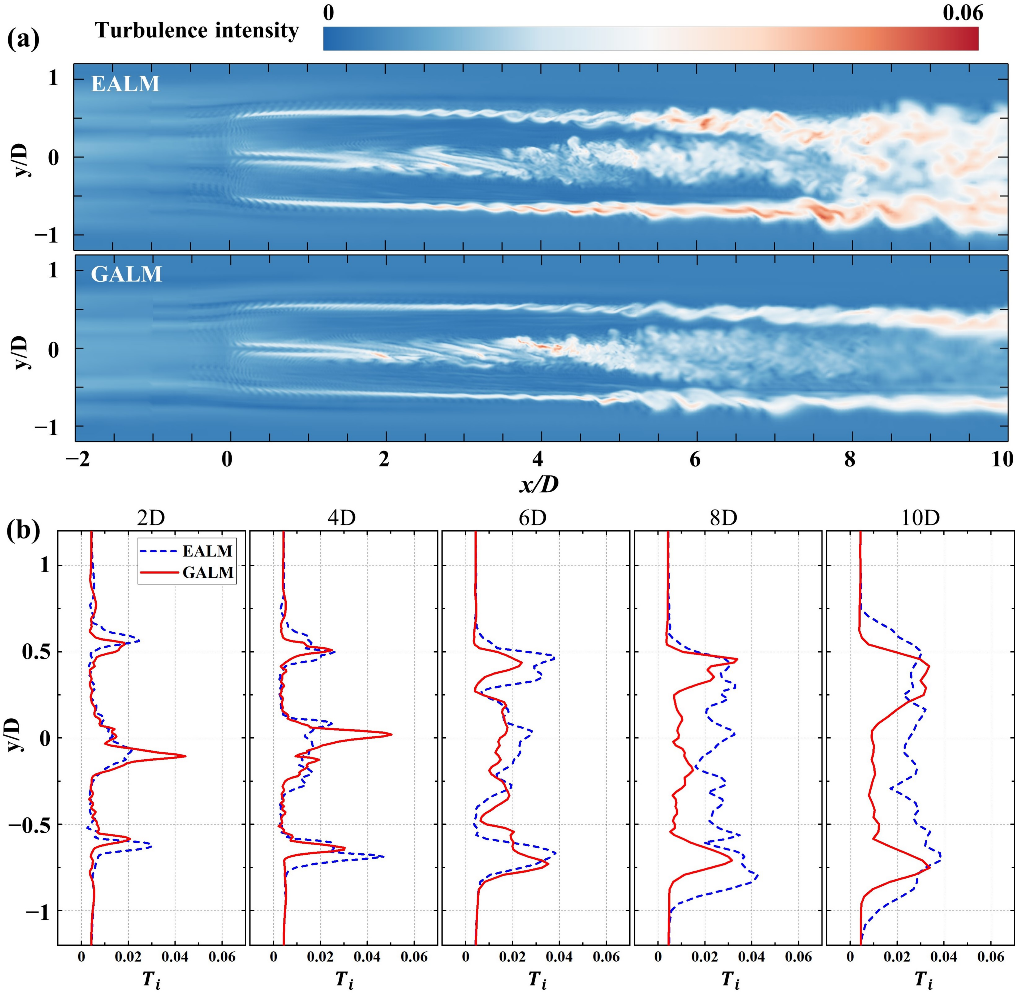

Figure 24. Comparative analysis of the turbulence intensity field in EALM and GALM: (**a**) The turbulence intensity contour (z = 0 m). (**b**) The turbulence intensity at hub height (z = 0 m). T_i is the turbulence intensity.

Figure 24b shows the turbulence intensity distribution curves plotted for each cross-section. It can be observed that the turbulence intensity of the linear model EALM is consistently lower than that of the nonlinear model GALM. As the wake evolves, this difference gradually increases, reaching its maximum around 8D downstream. Thereafter, the turbulence intensity of the linear model EALM begins to decrease, while the nonlinear model GALM continues to increase. High turbulence intensity facilitates mixing between the high-speed ambient flow and the low-speed wake in the far wake, accelerating the wake recovery process, inducing stronger instabilities and turbulence, and further enhancing the mixing effect. Additionally, the differences between the two models are more pronounced at the rotor tip compared to other regions. This may be attributed to differences in the aerodynamic force predictions of the two models. As the wake develops, this difference gradually propagates toward the rotor center. Ultimately, it affects the entire far-wake region.

Notably, the nonlinear model's rotor extracts less energy from the environment, resulting in a smaller velocity deficit in the wake, which theoretically should lead to higher velocity distribution and a smaller low-speed region in the far-wake region. However, due to blade bending–torsion deformation, the aerodynamic force predictions near the rotor tip are lower. This weakens the turbulent mixing effects induced by tip vortices in the far-wake region, slowing the wake recovery rate. Ultimately, this results in the formation of a larger low-speed region. Overall, for large flexible wind turbines, the effect of geometric nonlinearity on the wake cannot be ignored. Nonlinear bending–torsion coupling deformation significantly reduces the aerodynamic load in the blade tip region and the overall thrust coefficient of the wind turbine. This change further weakens the tip vortex intensity and slows down the recovery rate in the far-wake region.

5. Summary and Conclusions

This study presents a nonlinear aeroelastic coupling model based on the Actuator Line Model (ALM) and Geometrically Exact Beam Theory (GEBT), which utilizes large-eddy simulation (LES) to simulate the aerodynamic and elastic performance of flexible blades undergoing large geometric deformations. First, the simulation results of the NREL-5MW wind turbine were compared with those from other studies to validate the reliability of the model. Subsequently, its effectiveness in aeroelastic simulations for the IEA-15MW wind turbine is validated through comparison with OpenFAST software. The nonlinear aeroelastic model can accurately predict the aerodynamic response, blade structural deformation, and wake field behavior of large flexible wind turbines. Furthermore, by comparing with the linear structural model using the Euler–Bernoulli beam, this study investigates the effect of structural nonlinearity on the aeroelastic response and wake characteristics of wind turbines, leading to the following conclusions:

Under rated operating conditions, the nonlinear deformation of the blades leads to a reduction in the aerodynamic load and rotor performance of the wind turbine, with the impact on thrust being significantly greater than on power. The bending–torsion coupling effect leads to lower angle of attack (AOA), resulting in a significant decrease in aerodynamic load distribution, particularly near the blade tip. The nonlinear deformation of the blade has a significantly greater impact on the mean variation of aerodynamic loads than on their amplitude variation. Additionally, in terms of deformation, nonlinear deformation has a more pronounced impact on the edgewise deformation. The deformation distribution along the blade indicates that the linear model cannot effectively capture the bending–twist coupling nonlinear characteristics of highly flexible blades.

The nonlinear deformation of the blades not only affects the aerodynamic performance and rotor plane deformation but also alters the vortex structure, wake recovery, and turbulence intensity. In the near wake, the nonlinear model GALM shows a smaller velocity deficit. However, due to the bending–twist coupling nonlinear effects, the blade tip load is reduced, and the tip vortex strength significantly weakens, which slows down the mixing of the high-speed surrounding flow and the low-speed wake. This leads to a slower recovery of the wake velocity deficit. As a result, in the far-wake region, the velocity deficit in the nonlinear model GALM is larger than in the linear model EALM, and the expansion of the wake region is smaller. Blade nonlinear deformation reduces the wake recovery speed and intensity of large wind turbines. Additionally, the differences in turbulence intensity distribution are mainly observed in the far-wake region. The turbulence intensity in the linear model EALM is higher and more widely distributed, while in the nonlinear model

GALM, the intensity is lower and more concentrated around the rotor tip region. Blade nonlinear deformation slows down the momentum exchange within the wake region.

Overall, the nonlinear deformation of the blade has a significant impact on the aeroelastic response and wake characteristics of the large 15MW wind turbine. This includes a reduction in aerodynamic loads, a decline in aerodynamic performance, and changes in the blade deformation distribution. These changes, by altering the velocity difference and tip vortex, further influence the far-wake field, specifically manifested as a slower wake recovery and reduced turbulence intensity. These changes will significantly affect the optimization of wind farm layout. Furthermore, in the present work, the capability of the nonlinear aeroelastic model to simulate the aeroelastic performance and wake of large flexible blades has been validated, with a focus on studying how nonlinear blade deformation under uniform operating conditions affects the aeroelastic performance and wake characteristics of large flexible wind turbines. Future research should incorporate blade pitch control, platform motion, and more realistic inflow conditions to further enhance our understanding of blade nonlinear deformation and complex wake dynamics.

Author Contributions: Conceptualization, Z.C. and L.X.; methodology, Z.C. and L.X.; software, L.X. and W.L.; validation, L.X., Y.Q., W.L., and J.L.; formal analysis, Z.C. and Y.Q.; investigation, L.X.; resources, Z.C. and Y.Q.; data curation, L.X; writing—original draft preparation, L.X.; writing—review and editing, Z.C. and Y.Q.; visualization, Z.C. and L.X.; supervision, Z.C. and J.L.; project administration, Z.C. and W.L.; funding acquisition, Z.C. and Y.Q. All authors have read and agreed to the published version of the manuscript.

Funding: This research was funded by the National Natural Science Foundation of China (52301311) and 2023 DMU Navigation College First-Class Interdisciplinary Research Project (2023JXB13).

Institutional Review Board Statement: Not applicable

Informed Consent Statement: Not applicable

Data Availability Statement: No new data were created or analyzed in this study. Data sharing is not applicable to this article.

Conflicts of Interest: The authors declare no conflicts of interest.

References

1. Micallef, D.; Rezaeiha, A. Floating Offshore Wind Turbine Aerodynamics: Trends and Future Challenges. *Renew. Sustain. Energy Rev.* **2021**, *152*, 111696. [CrossRef]
2. Veers, P.; Bottasso, C.L.; Manuel, L.; Naughton, J.; Pao, L.; Paquette, J.; Robertson, A.; Robinson, M.; Ananthan, S.; Barlas, T.; et al. Grand Challenges in the Design, Manufacture, and Operation of Future Wind Turbine Systems. *Wind. Energy Sci.* **2023**, *8*, 1071–1131. [CrossRef]
3. Wang, Z.; Lu, Z.; Yi, W.; Hao, J.; Chen, Y. A Study of Nonlinear Aeroelastic Response of a Long Flexible Blade for the Horizontal Axis Wind Turbine. *Ocean Eng.* **2023**, *279*, 113660. [CrossRef]
4. Della Posta, G.; Leonardi, S.; Bernardini, M. A Two-Way Coupling Method for the Study of Aeroelastic Effects in Large Wind Turbines. *Renew. Energy* **2022**, *190*, 971–992. [CrossRef]
5. Wang, L.; Liu, X.; Kolios, A. State of the Art in the Aeroelasticity of Wind Turbine Blades: Aeroelastic Modelling. *Renew. Sustain. Energy Rev.* **2016**, *64*, 195–210. [CrossRef]
6. Zheng, J.; Wang, N.; Wan, D.; Strijhak, S. Numerical Investigations of Coupled Aeroelastic Performance of Wind Turbines by Elastic Actuator Line Model. *Appl. Energy* **2023**, *330*, 120361. [CrossRef]
7. Rezaei, M.M.; Behzad, M.; Haddadpour, H.; Moradi, H. Aeroelastic Analysis of a Rotating Wind Turbine Blade Using a Geometrically Exact Formulation. *Nonlinear Dyn.* **2017**, *89*, 2367–2392. [CrossRef]
8. Dose, B.; Rahimi, H.; Herráez, I.; Stoevesandt, B.; Peinke, J. Fluid-Structure Coupled Computations of the NREL 5 MW Wind Turbine by Means of CFD. *Renew. Energy* **2018**, *129*, 591–605. [CrossRef]
9. Leng, J.; Gao, Z.; Wu, M.C.; Guo, T.; Li, Y. A Fluid–Structure Interaction Model for Large Wind Turbines Based on Flexible Multibody Dynamics and Actuator Line Method. *J. Fluids Struct.* **2023**, *118*, 103857. [CrossRef]

10. Trigaux, F.; Chatelain, P.; Winckelmans, G. Investigation of Blade Flexibility Effects on the Loads and Wake of a 15 MW Wind Turbine Using a Flexible Actuator Line Method. *Wind Energy Sci.* **2024**, *9*, 1765–1789. [CrossRef]
11. Brown, K.; Houck, D.; Maniaci, D.; Westergaard, C.; Kelley, C. Accelerated Wind-Turbine Wake Recovery Through Actuation of the Tip-Vortex Instability. *AIAA J.* **2022**, *60*, 3298–3310. [CrossRef]
12. Amiri, M.M.; Shadman, M.; Estefen, S.F. A Review of Physical and Numerical Modeling Techniques for Horizontal-Axis Wind Turbine Wakes. *Renew. Sustain. Energy Rev.* **2024**, *193*, 114279. [CrossRef]
13. Chattot, J.J. Helicoidal Vortex Model for Wind Turbine Aeroelastic Simulation. *Comput. Struct.* **2007**, *85*, 1072–1079. [CrossRef]
14. Marten, D.; Lennie, M.; Pechlivanoglou, G.; Nayeri, C.N.; Paschereit, C.O. Implementation, Optimization and Validation of a Nonlinear Lifting Line Free Vortex Wake Module Within the Wind Turbine Simulation Code QBlade. *J. Eng. Gas Turbines Power* **2016**, *138*, 072601. [CrossRef]
15. Greco, L.; Testa, C. Wind Turbine Unsteady Aerodynamics and Performance by a Free-Wake Panel Method. *Renew. Energy* **2021**, *164*, 444–459. [CrossRef]
16. Yu, D.O.; Kwon, O.J. Predicting Wind Turbine Blade Loads and Aeroelastic Response Using a Coupled CFD–CSD Method. *Renew. Energy* **2014**, *70*, 184–196. [CrossRef]
17. Lei, H.; Zhou, D.; Lu, J.; Chen, C.; Han, Z.; Bao, Y. The Impact of Pitch Motion of a Platform on the Aerodynamic Performance of a Floating Vertical Axis Wind Turbine. *Energy* **2017**, *119*, 369–383. [CrossRef]
18. Sorensen, J.N.; Shen, W.Z. Numerical Modeling of Wind Turbine Wakes. *J. Fluids Eng.* **2002**, *124*, 393–399. [CrossRef]
19. Churchfield, M.J.; Lee, S.; Michalakes, J.; Moriarty, P.J. A Numerical Study of the Effects of Atmospheric and Wake Turbulence on Wind Turbine Dynamics. *J. Turbul.* **2012**, *13*, N14. [CrossRef]
20. Xu, S.; Zhuang, T.; Zhao, W.; Wan, D. Numerical Investigation of Aerodynamic Responses and Wake Characteristics of a Floating Offshore Wind Turbine under Atmospheric Boundary Layer Inflows. *Ocean Eng.* **2023**, *279*, 114527. [CrossRef]
21. Onel, H.C.; Tuncer, I.H. Investigation of Wind Turbine Wakes and Wake Recovery in a Tandem Configuration Using Actuator Line Model with LES. *Comput. Fluids* **2021**, *220*, 104872. [CrossRef]
22. Zhao, M.; Chen, S.; Wang, K.; Wu, X.; Zha, R. Effect of the Yaw Angle on the Aerodynamics of Two Tandem Wind Turbines by Considering a Dual-Rotor Wind Turbine in Front. *Ocean Eng.* **2023**, *283*, 114974. [CrossRef]
23. Meng, H.; Lien, F.S.; Li, L. Elastic Actuator Line Modelling for Wake-Induced Fatigue Analysis of Horizontal Axis Wind Turbine Blade. *Renew. Energy* **2018**, *116*, 423–437. [CrossRef]
24. Yu, Z.; Ma, Q.; Zheng, X.; Liao, K.; Sun, H.; Khayyer, A. A Hybrid Numerical Model for Simulating Aero-Elastic-Hydro-Mooring-Wake Dynamic Responses of Floating Offshore Wind Turbine. *Ocean Eng.* **2023**, *268*, 113050. [CrossRef]
25. Hansen, M.; Sørensen, J.; Voutsinas, S.; Sørensen, N.; Madsen, H.A. State of the Art in Wind Turbine Aerodynamics and Aeroelasticity. *Prog. Aerosp. Sci.* **2006**, *42*, 285–330. [CrossRef]
26. Wang, L.; Liu, X.; Renevier, N.; Stables, M.; Hall, G.M. Nonlinear Aeroelastic Modelling for Wind Turbine Blades Based on Blade Element Momentum Theory and Geometrically Exact Beam Theory. *Energy* **2014**, *76*, 487–501. [CrossRef]
27. Sieros, G.; Chaviaropoulos, P.; Sørensen, J.D.; Bulder, B.H.; Jamieson, P. Upscaling Wind Turbines: Theoretical and Practical Aspects and Their Impact on the Cost of Energy. *Wind Energy* **2012**, *15*, 3–17. [CrossRef]
28. Panteli, A.N.; Manolas, D.I.; Riziotis, V.A.; Spiliopoulos, K.V. Comparative Study of Two Geometrically Non-Linear Beam Approaches for the Coupled Wind Turbine System. *J. Wind. Eng. Ind. Aerodyn.* **2022**, *231*, 105231. [CrossRef]
29. Lapa, G.V.P.; Gay Neto, A.; Franzini, G.R. Effects of Blade Torsion on IEA 15MW Turbine Rotor Operation. *Renew. Energy* **2023**, *219*, 119546. [CrossRef]
30. Qian, X.; Zhang, B.; Gao, Z.; Wang, T.; Zhang, L.; Li, Y. Flutter Limit Optimization of Offshore Wind Turbine Blades Considering Different Control and Structural Parameters. *Ocean Eng.* **2024**, *310*, 118558. [CrossRef]
31. Wang, Q.; Sprague, M.A.; Jonkman, J.; Johnson, N.; Jonkman, B. BeamDyn: A High-fidelity Wind Turbine Blade Solver in the FAST Modular Framework. *Wind Energy* **2017**, *20*, 1439–1462. [CrossRef]
32. Sabale, A.K.; Gopal, N.K.V. Nonlinear Aeroelastic Analysis of Large Wind Turbines Under Turbulent Wind Conditions. *AIAA J.* **2019**, *57*, 4416–4432. [CrossRef]
33. Liu, Y.; Xiao, Q.; Incecik, A.; Peyrard, C. Aeroelastic Analysis of a Floating Offshore Wind Turbine in Platform-induced Surge Motion Using a Fully Coupled CFD-MBD Method. *Wind Energy* **2019**, *22*, 1–20. [CrossRef]
34. Höning, L.; Lukassen, L.J.; Stoevesandt, B.; Herráez, I. Influence of Rotor Blade Flexibility on the Near-Wake Behavior of the NREL 5 MW Wind Turbine. *Wind Energy Sci.* **2024**, *9*, 203–218. [CrossRef]
35. Ma, Z.; Zeng, P.; Lei, L. Analysis of the Coupled Aeroelastic Wake Behavior of Wind Turbine. *J. Fluids Struct.* **2019**, *84*, 466–484. [CrossRef]
36. Huang, Y.; Yang, X.; Zhao, W.; Wan, D. Aeroelastic Analysis of Wind Turbine under Diverse Inflow Conditions. *Ocean Eng.* **2024**, *307*, 118235. [CrossRef]
37. Santoni, C.; Khosronejad, A.; Yang, X.; Seiler, P.; Sotiropoulos, F. Coupling Turbulent Flow with Blade Aeroelastics and Control Modules in Large-Eddy Simulation of Utility-Scale Wind Turbines. *Phys. Fluids* **2023**, *35*, 015140. [CrossRef]

38. Fleming, P.A.; Gebraad, P.M.; Lee, S.; Van Wingerden, J.W.; Johnson, K.; Churchfield, M.; Michalakes, J.; Spalart, P.; Moriarty, P. Evaluating Techniques for Redirecting Turbine Wakes Using SOWFA. *Renew. Energy* **2014**, *70*, 211–218. https://doi.or/10.1016/j.renene.2014.02.015. [CrossRef]
39. Muscari, C.; Giordani, R.; Schito, P. On Wind Turbine Structural Stiffness Influence on Wake Flow. *J. Fluids Struct.* **2023**, *118*, 103862. [CrossRef]
40. Jonkman, J. The New Modularization Framework for the FAST Wind Turbine CAE Tool. In Proceedings of the 51st AIAA Aerospace Sciences Meeting Including the New Horizons Forum and Aerospace Exposition, Grapevine, TX, USA, 7–10 January 2013; p. 202. [CrossRef]
41. Churchfield, M.J.; Schreck, S.J.; Martinez, L.A.; Meneveau, C.; Spalart, P.R. An Advanced Actuator Line Method for Wind Energy Applications and Beyond. In Proceedings of the 35th Wind Energy Symposium, Grapevine, TX, USA, 9–13 January 2017; p. 1998. [CrossRef]
42. Martínez-Tossas, L.A.; Churchfield, M.J.; Meneveau, C. A Highly Resolved Large-Eddy Simulation of a Wind Turbine Using an Actuator Line Model with Optimal Body Force Projection. *J. Phys. Conf. Ser.* **2016**, *753*, 082014. [CrossRef]
43. Muscari, C.; Schito, P.; Viré, A.; Zasso, A.; Van Wingerden, J.W. The Effective Velocity Model: An Improved Approach to Velocity Sampling in Actuator Line Models. *Wind Energy* **2024**, *27*, 447–462. [CrossRef]
44. Shen, W.Z.; Mikkelsen, R.; Sørensen, J.N.; Bak, C. Tip Loss Corrections for Wind Turbine Computations. *Wind Energy* **2005**, *8*, 457–475. [CrossRef]
45. Bauchau, O.A. *Flexible Multibody Dynamics*; Solid Mechanics and Its Applications; Springer: Dordrecht, The Netherlands, 2011; Volume 176. [CrossRef]
46. Gao, Z.; Li, Y.; Wang, T.; Shen, W.; Zheng, X.; Pröbsting, S.; Li, D.; Li, R. Modelling the Nacelle Wake of a Horizontal-Axis Wind Turbine under Different Yaw Conditions. *Renew. Energy* **2021**, *172*, 263–275. [CrossRef]
47. Jha, P.K.; Schmitz, S. Actuator Curve Embedding—An Advanced Actuator Line Model. *J. Fluid Mech.* **2018**, *834*, R2. [CrossRef]
48. Martínez-Tossas, L.A.; Churchfield, M.J.; Leonardi, S. Large Eddy Simulations of the Flow Past Wind Turbines: Actuator Line and Disk Modeling: LES of the Flow Past Wind Turbines: Actuator Line and Disk Modeling. *Wind Energy* **2015**, *18*, 1047–1060. [CrossRef]
49. Yang, L.; Liao, K.; Ma, Q.; Khayyer, A.; Sun, H. Coupled Aero-Servo-Elastic Method for Floating Offshore Wind Turbine Wake Analysis. *Ocean Eng.* **2024**, *307*, 118108. [CrossRef]
50. Ji, R.; Sun, K.; Zhang, J.; Zhu, R.; Wang, S. A Novel Actuator Line-Immersed Boundary (AL-IB) Hybrid Approach for Wake Characteristics Prediction of a Horizontal-Axis Wind Turbine. *Energy Convers. Manag.* **2022**, *253*, 115193. [CrossRef]
51. Liu, Y. The Effect of Vertical Arrangement on Performance and Wake Characteristics of Two Tandem Offshore Wind Turbines under Various Operating Conditions. *Energy Convers. Manag.* **2023**, *278*, 116743. [CrossRef]
52. Liu, L.; Franceschini, L.; Oliveira, D.F.; Galeazzo, F.C.; Carmo, B.S.; Stevens, R.J.A.M. Evaluating the Accuracy of the Actuator Line Model against Blade Element Momentum Theory in Uniform Inflow. *Wind Energy* **2022**, *25*, 1046–1059. [CrossRef]
53. Melani, P.F.; Mohamed, O.S.; Cioni, S.; Balduzzi, F.; Bianchini, A. An Insight into the Capability of the Actuator Line Method to Resolve Tip Vortices. *Wind Energy Sci.* **2024**, *9*, 601–622. [CrossRef]
54. Jonkman, J.; Butterfield, S.; Musial, W.; Scott, G. *Definition of a 5-MW Reference Wind Turbine for Offshore System Development*; Technical Report; National Renewable Energy Laboratory.(NREL): Golden, CO, USA, 2009. [CrossRef]
55. Sun, W. Passive Aeroelastic Study of Large and Flexible Wind Turbine Blades for Load Reduction. *Structures* **2023**, *58*, 105331. [CrossRef]